Modeling-Backed Microwave Imaging in Closed Systems: Reconstruction of a Spherical Inhomogeneity

A Major Qualifying Project

Submitted to the Faculty of the
WORCESTER POLYTECHNIC INSTITUTE
in partial fulfilment of the requires for the
Degree of Bachelor of Science
by

Taylor J. York

April 25, 2017

Advised by:
Professor Vadim V. Yakovlev

Abstract

Despite a wide practical use of sophisticated imaging devices based on ultrasound, X-Ray, and MRI, the need of safe, accurate and cost-efficient imaging technologies is still acute. This project addresses the problem of development of reliable and robust computational techniques required for processing of data in microwave imaging performed inside closed metal cavities. We outline a computational procedure for the use in microwave imaging of a spherical inhomogeneity in a dielectric sample. This procedure utilizes an artificial neural network capable of full reconstructing geometrical and material parameters of the inclusion. The network uses data from the FDTD model of a multiport microwave system. A series of computational experiments is reported for the standard four-port waveguide element (known as a Magic Tees Junction) containing a rectangular Teflon sample with a hidden dielectric or metal inclusion. The error in reconstruction of four geometrical parameters of a dielectric sphere is shown to be on the level of 1.7-3.3%, whereas the error in determination of complex permittivity of the inclusion is about 9.8%. The project makes a solid theoretical background for the upcoming experimental program exploring the resources of multiport closed systems for practical microwave imaging applications.

This Major Qualifying Project was sponsored by MACOM.

Acknowledgements

I would like to thank the following people who, without their help, none of this project and its future would be possible:

- Dr. Vadim V. Yakovlev, Worcester Polytechnic Institute, Worcester, MA – for the opportunity to embark on this project;
- MaCom Technology Solution, MACOM – for the sponsorship of the experimental program;
- The Computational Electromagnetics Research Laboratory, McMaster University, Hamilton, ON, Canada – for their cooperation in development of the experimental setup;
- Dr. Alexander V. Brovko, Saratov State Technical University, Saratov, Russia and Dr. Ethan K. Murphy, Dartmouth College, Hanover, NH – for help with the theory and practice of ANNs;
- Roger Steele (PH) and Thomas Partington (CE), Worcester Polytechnic Institute, Worcester, MA – for the production of the Teflon samples with spherical inclusions;
- Jonathan Brousseau, MACOM – for management of the production of the WR340 experimental system;
- Dr. Alexander Beaverstone, McMaster University – for consultancy regarding the technical aspects of the experimental program
- My friends and family – for supporting me throughout my academic career at Worcester Polytechnic Institute.

Table of Contents

List of Figures and Tables

1. Introduction

1.1 Non-Destructive Evaluation, Testing and Microwave Imaging

Non-Destructive Evaluation (NDE) and Non-Destructive Testing (NDT) are a variety of techniques of scanning the interior of an object without destroying it. This is conducted to determine the properties of the object by checking for the presence of defects, inclusions, non-uniformities, etc. Among the popular NDE/NDT techniques are, for example, X-Rays, ultrasound, and Magnetic Resonance Imaging (MRI). They are very popular in multiple medical applications; however, all of them have their own drawback. X-rays are ionizing irradiation, which, in notable doses, may be harmful for living organisms. Ultrasound is safe for the tissues, but are not precise enough for many practical needs. The MRI equipment is very expensive and has a limited range of possible uses [1]-[3]. So, recently, many extended and in-depth studies have been conducted to develop new NDE/NDT techniques, which would perform safer, more accurate, and more cost-effective evaluations.

Microwave imaging is one of these techniques, and is currently under extensive development towards many different applications [4]-[5] such as medical diagnostics (including detection of
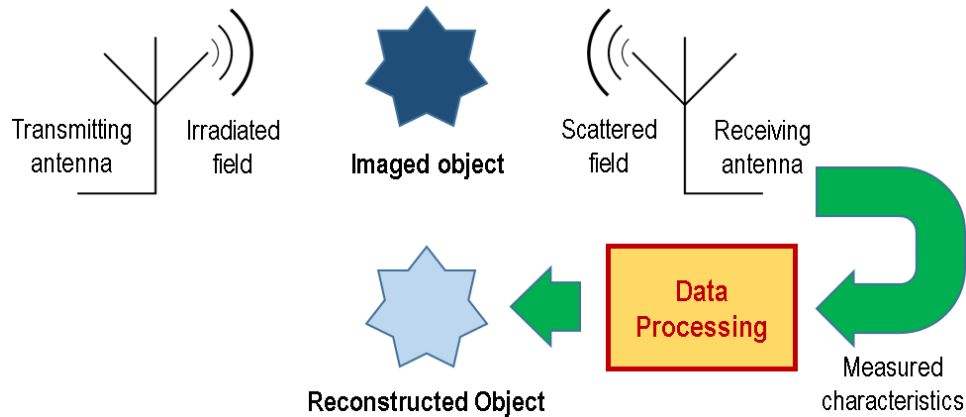
Figure 1.1. General characterization of the process of microwave imaging.

inhomogeneities in distribution of tissues) [6]-[7], NDT of defects and cracks in construction materials [8], composite panels [9], wood slabs [10], and detection of concealed weapons [11], and through-wall imaging [12]. Microwave imaging is traditionally conducted in open space and requires the use of antennas to transmit and receive the electromagnetic signal. Shown in Figure 1.1, the process of microwave imaging is as follows. A transmitting antenna sends an irradiated field that comes into contact with the imaged object. That object scatters the field, and a receiving antenna receives the scattered field. Measured characteristics are determined from the information received from the scattered field and then sent into data processing. The data processing deciphers this information in order to reconstruct the parameters and create a visualization of the imaged object.

Current practices benefit from the progress in theoretical studies of the inverse problems in free space (e.g., [13]). However, experimental implementations in open space are typically quite complicated, and it is difficult to obtain accurate measurements. NDE/NDT functions can be also performed in closed systems (like resonators and waveguides), and it has been shown that in this case microwave imaging may offer simpler implementations and measurements [14]. Yet, due to the complexity of the theoretical aspects of the related inverse problems [15]-[17], the technology of microwave imaging in closed systems has not been sufficiently developed. There are very few reports on the practical use of this methodology, for example, in reconstruction of voids in concrete structures or bricks [18], detection of defects in wood slabs

[10] and composite panels [9], detection of porosity in ceramics and molded rubber [19], monitoring of inhomogeneities in food products [20], and in some medical diagnostics [21].

Recently, there has been a series of papers reporting on the development of advanced numerical techniques for modeling scenarios related to the microwave imaging in closed systems [22]-[25]. The full-wave 3-D Finite-Difference Time-Domain (FDTD) technique [26]-[27] has been found to be the tool most convenient and powerful in applicable numerical analysis [28]-[29]. It has been shown that the large amount of information about those systems can be used for numerically solving corresponding inverse problems. To this end, the Artificial Neural Network (ANN) technique [30]-[31] has been found to be an efficient and sufficiently accurate method.

For instance, two-dimensional profiles of complex permittivity of dielectric samples were reconstructed in [12], and volume fraction of solid material in dielectric powder was determined in [32]. Furthermore, a technique for the detection of a position and a size of a spherical inclusion within a dielectric sample was proposed in [33]. In these three papers, NDT functions were performed in a two-port waveguide system; that applied remarkable limitation on the amount of information about the tested sample that can be gathered from measurement. It has been later suggested that this barrier can be overcome by introducing a close cavity with additional ports; for example, in [34], a 6-port device was successfully used to reconstruct three-dimensional profiles of complex permittivity.

Microwave imaging of an inclusion in a dielectric sample is a problem which may be relevant to many applications. However, the technique developed in [33] has rather limited capabilities. It necessarily requires consideration of three orientations of the sample in the waveguide, and that could be practically inconvenient. It also assumes that the complex permittivity of the inclusion is known, but in many scenarios, this is not the case. This project addresses both these issues. It introduces a significant extension of capabilities of the approach reported in [33] by placing the tested sample in a multi-port system (similar to [34]) and introducing an appropriate ANN which does not require different orientations of the tested sample and is able to determine its material parameters.

3

1.2 Project Objectives

As follows from previously stated, the objectives of this project were to:

1) Show the capabilities of a practical multiport closed system in detecting the coordinates and radius of spherical inclusion without changing orientation of the tested object.

2) Investigate the options in using the chosen multiport system in detecting, along with the coordinates and the radius, dielectric constant and the loss factor of the inclusion.

3) Improve the accuracy of the reconstruction aiming to make the technique operational with a prospective experimental implementation.

2. Methodology

2.1 Biological Neurons and Their Models

Biological neurons are structural elements of the brain that control the flow of informational impulses through the human nervous system to turn sensory inputs into respective action/reaction outputs. They come in many different shapes and sizes, but each individual neuron is comprised of several key parts that allow for the appropriate transfer of these impulses. As shown in Figure 2.1, the biological neuron consists of Dendrites, a Soma, Nucleus, Axon, Axon Branches, and Axon terminals. Dendrites are branches of a neuron that take in external inputs in the form of impulses. These impulses are sent along the dendrites of the neuron to nucleus of the neuron through the cell body (soma). The nucleus then processes the signal by calling on its stored memory and weighing the importance of sending signals to each of its neighboring neurons. Once the nucleus decides the destination, the impulse is sent along the axon of the neuron to the branches of the axon. From there the impulse is passed along from the axon's terminals across synaptic spaces to the neighboring neuron's dendrites [30].
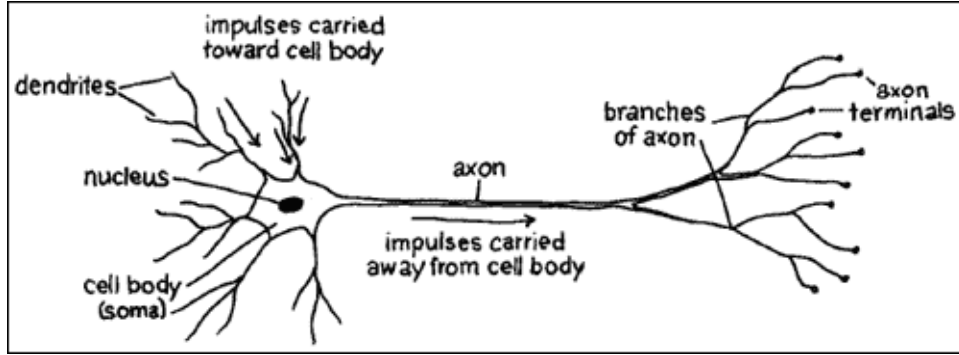
Figure 2.1. Parts of a biological neuron.

The process in which an impulse is carried through a neuron can be modeled artificially and broken down into five parts as illustrated in Figure 2.2. First, the model represents each dendrite of a neuron receiving a signal with x_j, $j = 1,...,n$, where j denotes the dendrite connected to a neuron k. Each x_j is subjected to a synaptic weight multiplier w_{kj}. The first subscript refers to the neuron in which the weight is connected to, while the second subscript refers to the dendrite/input which belongs to that weight. Steps two through four model the decision-making processes of the nucleus of a neuron. An adder is invoked in the form of a summation junction in which the weighted input signals are summed. Next, an external bias denoted b_k has an effect on increasing or decreasing the net input and whether it is interpreted as positive or negative. Then the result is sent to an activation function. The latter, denoted by $\boldsymbol{\phi}(v_k)$, determines the output in terms of the induced field v_k, limiting the amplitude to be constrained within either the interval [0, 1], or [-1, 1]. Lastly, in step five, after being constrained the information of the output signal denoted y_k is sent on to the next neuron in the system and the process is repeated until a desired outcome is achieved.

Following [31], in mathematical terms, the summation junction of neuron k can be written as:

$$u_k = \sum_{j=1}^{n} w_{kj} x_j \, , \tag{2.1}$$

and, in addition, the output of the neuron as:

$$y_k = \boldsymbol{\phi}(u_k + b_k) \, , \tag{2.2}$$

where $x_1, x_2, ..., x_n$ are the input signals, $w_{k1}, w_{k2}, ..., w_{kn}$ are the synaptic weights of each input signal, u_k is the linear combiner output from the summation junction. Where $\boldsymbol{\phi}(*)$ is the activation function, and y_k is
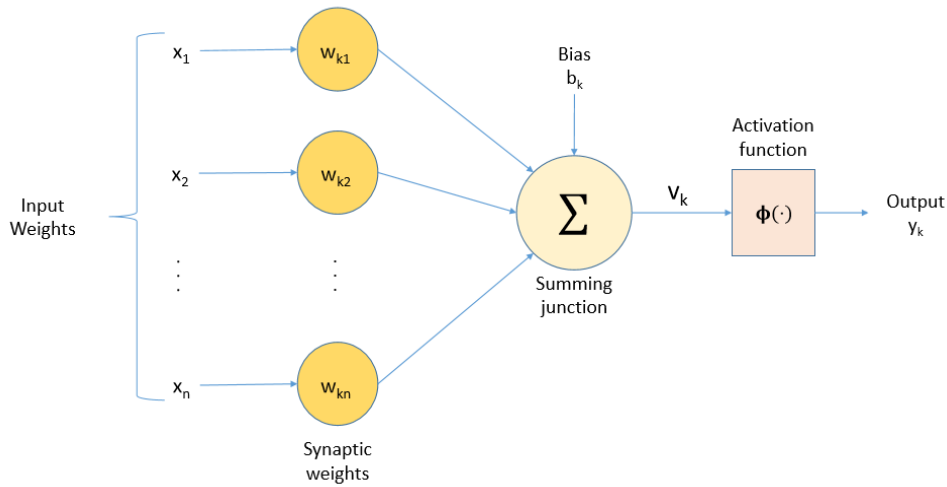
Figure 2.2. Nonlinear model of an artificial neuron.

signal of the neuron. The introduction of the bias has an affine transformation to the output u_k of the linear combiner represented by:

$$v_k = u_k + b_k \tag{2.3}$$

Accounting for the bias's presence gives:

$$v_k = \sum_{j=0}^{n} w_{kj} x_j \tag{2.4}$$

and the output y_k can be explained as:

$$y_k = \phi(v_k) \tag{2.5}$$

The bias applies a simple alteration of (2.1) by moving the starting point from $j = 1$ to $j = 0$ as shown in (2.4).

The activation function $\phi(*)$ can be represented in multiple manners, for instance, as the sigmoid function offering a good balance between both linear and nonlinear behavior. An example of the sigmoid function is the logistic function:

$$\phi(v) = \frac{1}{1+\exp(-av)} \tag{2.6}$$

where a is the slope parameter of the sigmoid function. Since this function ranges from 0 to +1, it is important to note that there are times when negative values are necessary for consideration. For these
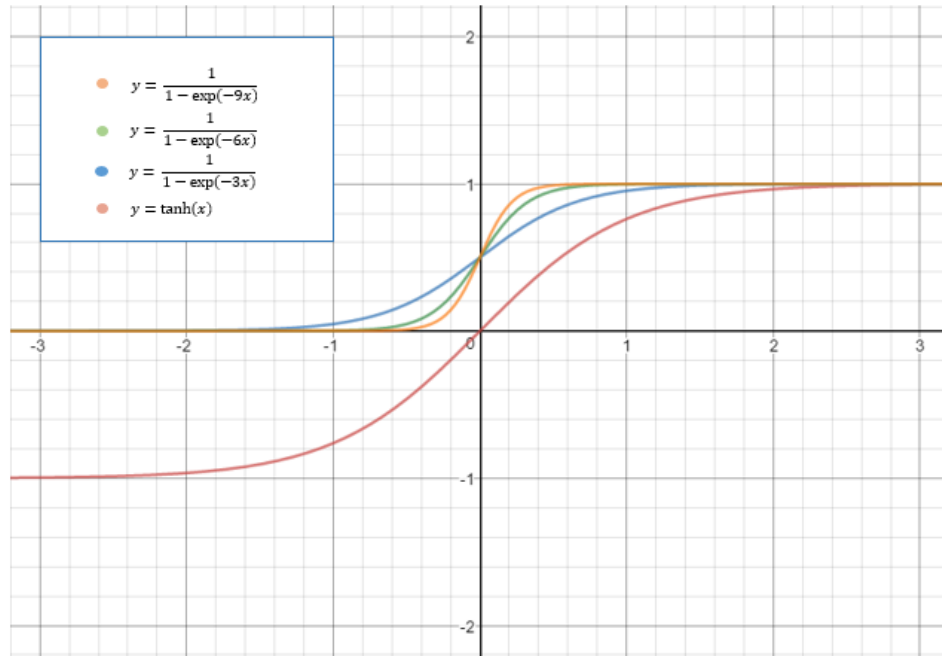
Figure 2.3. Graph of sigmoid and hyperbolic tangent functions

cases the use of a hyperbolic tangent function

$$\boldsymbol{\phi}(v) = \tanh(v) \qquad (2.7)$$

may be necessary. The graphs of both the sigmoid and hyperbolic tangent functions are shown in Figure 2.3.

This mathematical model is the basis to the construction of an artificial neural network (ANN). ANNs are parallel computational models comprised of densely interconnected adaptive processing units [30]. ANN computation techniques attempt to mimic the memory and pattern recognition capabilities of biological neuron systems. This is achieved by imitating the brain's neuron structures and its learning capabilities through the training of the artificial neurons of an ANN.

2.2 Network Architectures

As mentioned above, an artificial neuron can be used to model functions of an individual biological neuron. When multiple artificial neurons are combined for computational use, they create a network of neurons that can be used to mimic diverse structures of biological neural networks. ANN structures depend on the amount of computational power needed to provide a desired result; they can be classified into different groups composed by arrangement of neurons and the connection patterns of the layers. Three most popular groups are feedforward (error backpropagation networks), feedback (recurrent neural networks), and self-organizing (Kohonen) networks [30], [31]. In terms of number of neuron layers, feedforward networks can be characterized as follows:

Single-Layer Feedforward Networks. This is the simplest form of ANN architecture as it has only inputs that feed directly into the output nodes, but not vice versa. Thus, this network is only feedforward. It is shown in Figure 2.4(a) for the case with three nodes in both the input and output layers. This network is called a single layer network, where the single layer being referred to is the output layer of computational neurons. (The input layer is not counted as no computations are conducted in that layer.)

Multilayer Feedforward Networks. This network adds the presence of one or more hidden layers of neurons. Shown in Figure 2.4(b), each neuron in the hidden layers is used to perform a useful computation before sending the information on to the next neuron. When large amounts of hidden layers are introduced, the network becomes able to work with large data sets. In multilayer networks, the inputs of the input layer feed the neurons of the first hidden layer, which feed in turn the next hidden layer and so on until the final output layer is reached. It is important to note that the inputs of each layer of neurons are fed only by the outputs of the layer preceding that layer. Figure 2.4 (b) is comprised of an input layer of six inputs, one hidden layer of three neurons, and an output layer or two neurons. For notation purposes, this network may be labeled a 6-3-2 network. It is fully connected in the sense that all of the inputs in the input layer connect to all of the neurons in the hidden layer, which are connected to all of the neurons in the output layer.
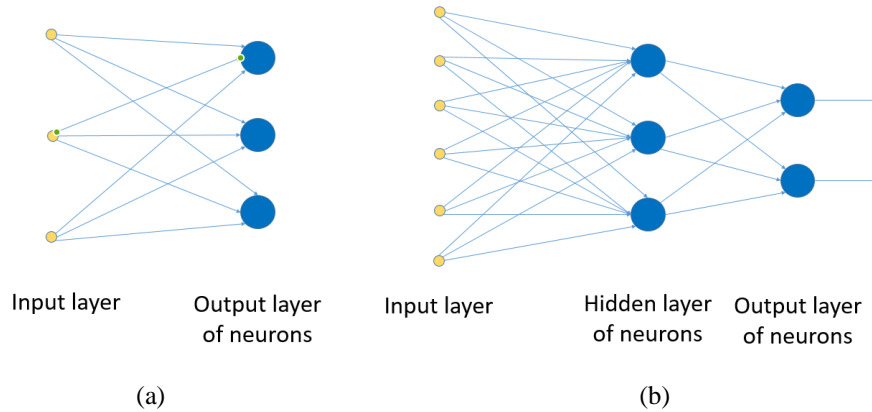
Figure 2.4. Single layer network (a) and multilayer network with one hidden layer (b).

2.3 Training and Using Artificial Neural Networks

Training of an ANN is also comparable to the process in which a neuron learns and stores information. This process is similar to when a child is being taught early in his/her life. When the child encounters a new input, e.g., the shape of a square, the child takes input information through his senses of sight (observing the shape) and through his hearing (receiving the name of the shape). The child is shown sets of squares to permanently learn the associations of the shape and finally is tested on what the shape is by placing the square in a set of shapes and having to identify it.

ANNs work in a similar way. As shown in Figure 2.5, first, a database is chosen to work with. From this database, all of the initial inputs and outputs are sorted and organized into vectors, and an ANN architecture is then designed/chosen to work with the data. Next, the ANN is run with the data to produce a response. This response is compared to the actual known data to compute the error between the two and if the error is large enough, the network's weights are tuned and the input data is applied again. This process repeats until the output's error is within the predetermined acceptable margin. ANN training takes place with the use of P points in the data sets. This is where most weights are tuned. The ANN weights can be further tuned with Q cross validation points so that an optimal radius can be determined. The process of
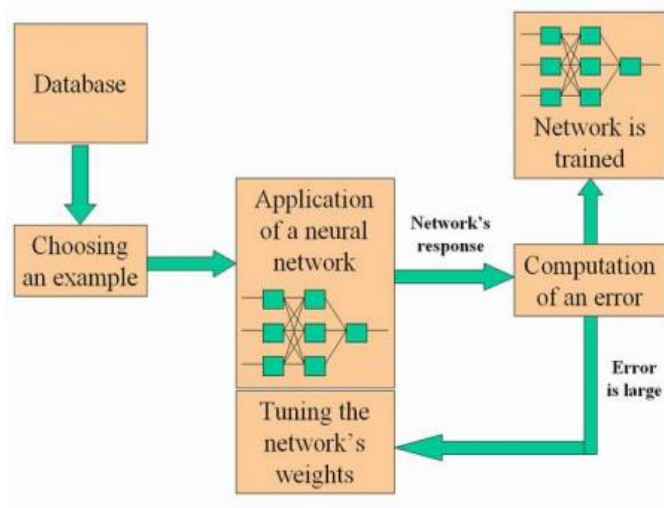
Figure 2.5. Process of training a neural network.

training continues until the error is deemed sufficiently low and the optimal tuned weights are found. Once this is achieved, then the training is complete.

When the neural network is well trained, it can be applied to solve problems and generate right reactions to newly introduced data; this process is illustrated in Figure 2.6.

In mathematical terms, the training process can be represented as follows. First, input-output are partitioned into pairs for training

$$f_1 = \{ \mathbf{X}^{(1)}, \mathbf{Y}^{(1)} \} , \tag{2.8}$$

and pairs for testing

$$f_2 = \{ \mathbf{X}^{(2)}, \mathbf{Y}^{(2)} \} , \tag{2.9}$$

where $\mathbf{X}^{(i)}$ is a matrix of input column vectors $\mathbf{X}_1, \ldots, \mathbf{X}_n$ and $\mathbf{Y}^{(i)}$ is the matrix of output column vectors $\mathbf{Y}_1, \ldots, \mathbf{Y}_n$. Second, a neural network of certain structure (depending on amount and type of data) is applied to the training input. Third, a computation of an error is performed using a zero error technique employed to determine the error between the training data and the testing data [30]. This is done by using a least squares approach to attempt to minimize the error. This is written as

$$\mathbf{E}(\mathbf{W}) = \frac{1}{2} \| \mathbf{Y}^{(1)} - \boldsymbol{\alpha} \|_2^2 = \frac{1}{2} \left(\mathbf{Y}^{(1)} - \boldsymbol{\alpha} \right)^T \left(\mathbf{Y}^{(1)} - \boldsymbol{\alpha} \right), \tag{2.10}$$

11
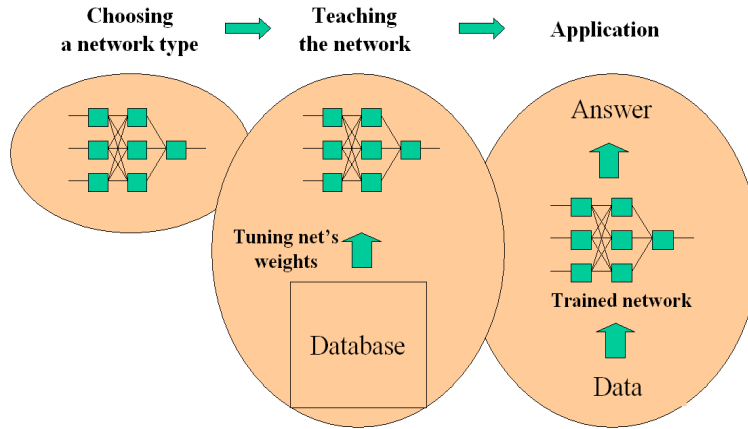
Figure 2.6. Flow chart illustrating the use of a neural network in a particular application.

where $\mathbf{E}(\mathbf{W})$ is the error and α is the function associated with the ANN structure. From there, (2.10) is minimized with respect to the weights $\mathbf{W}$ in order to find the optimal tuned weights (written as $\hat{\mathbf{W}}$). To solve this error equation, most ANNs must invoke an iterative method for non-linear optimization while in others cases ANN have a direct linear solution. Once the error function is solved, and the optimal tuned weights are found, the network is considered trained.

ANN training can be conducted in different ways, e.g., using the so-called *supervised* or *unsupervised* training. Under supervised training, the network is trained with the use of training data and is tested with the use of testing data. Then once the test data has been run through, the output is compared to the correct test outputs to determine if the system is trained. In unsupervised learning the goal is to optimize some criterion or performance function defined in terms of the output activity of the units in the network. This allows the network to determine when training is complete without the need of external help [30]-[31].

Therefore, the general approach to problem solving with ANN can be described as follows:

(a) Identifying the system's design parameters and core characteristics;

(b) Building a suitable ANN (by choosing a number of layers, a number of neurons in the hidden layers, etc.);

(c) Retrieve data about the system (type of math model and modeling software);

(d) Train the network with known data and test it with other known data;

12

(e) If the output of testing (step (d)) is satisfactory, give the ANN a question about the design parameters to receive an answer.

2.4 Electromagnetic Modeling

2.4.1 FDTD Technique

When an ANN is used for computer-aided design of an applied microwave imaging system, the network, in principle, would be expected to be trained by massive experimental data characterizing operational properties of that system. However, accurate measurements are technically challenging there, and post-processing of measured characteristics (and thus preparation of properly structured data) is a complicated and time-consuming business. It was suggested [12], [32]-[34] that ANN techniques can be practical for some closed systems as they can be sufficiently adequately represented by data generated from accurate numerical simulation. This data can be used for ANN training and testing – as in the second block in Figure 2.6. If the ANN is structured the way that it contains the parameters of the imaged hidden inclusion in the output layer, this network's response could be made a part of modeling-backed microwave imaging procedure. Required experiment in this case is reduced to a single measurement of quantities involved in modeling: when presented to the trained ANN (as in the third block in Figure 2.6), that data would invoke the "answer" to the "question" about the reconstructed parameters of the imaged sample.

This project follows this perception and relies on electromagnetic modeling results obtained with help of the Finite-Difference-Time-Domain (FDTD) method [26]-[27]. This method is based on the direct application of the central difference formula to both spatial and temporal derivatives in Maxwell's equations and their transformation to explicit expressions for the electric and magnetic field components on the grid of interlaced cells where the spatial increments are represented by $\delta = \Delta x = \Delta y = \Delta z$ and the time increment is given by Δt.

To ensure accuracy of the results δ must be small in comparison with the wavelength; a generally accepted standard is that δ should be no more than $\lambda/10$. The spatial cells should be also small enough in order to sufficiently accurately represent the shape of small and curvilinear objects involved in the scenario.

To keep the FDTD scheme stable, Δt and δ must also satisfy the Courant stability condition [26], [27]:

$$\Delta t \leq \frac{\delta}{c\sqrt{3}}. \tag{2.11}$$

A crucial practical consequence of this condition is that a reduction of a cell size δ requires a reduction in the corresponding time step Δt. This means that, in a non-uniform mesh, the smallest cell dictates the time step and thus enforces extension of the computational time.

The commonly acknowledged advantages of the FDTD technique include [29], [35]:

o Conceptual simplicity; conditions for clear and direct interpretations of the results;

o Absence of requirement to solve algebraic problems with huge matrices (and thus to use computationally expensive matrix inversions or iterative methods);

o Modest requirements for computer memory (which is used in sequential order);

o Predictability of computing time for any particular problem: with N^3 FDTD cells, it is always proportional to N^4 (while, for example, in the finite element method (FEM), it is proportional to $N^4 \ldots N^6$);

o Due to Fourier Transform (being a part of the FDTD technique), a single computation is needed for a frequency interval; multiple solutions for all frequencies of interest (inevitable, e.g., in the FEM in frequency domain) are not required.

The drawback of the classical FDTD technique, i.e., the grid of single-medium rectangular cells (the so-called "stair-case grid"), can be overcome in its conformal version [29]. In the conformal mesh, a cell can be filled with two different media with a linear boundary between them. In this case, a higher accuracy of spatial approximation can be reached without dramatically increasing the number of cells.

2.4.2 FDTD Modeling Software

In this project, the 3D conformal FDTD modeling software *QuickWave* [36] is used for simulation of the key characteristics of the 4-port waveguide structure considered as a prototype of a closed multi-port microwave imaging system. The simulator is used for determining magnitudes and phases of the reflection and transmission characteristics. More specifically, in port n ($n = 1, .., 4$), *QuickWave* computes the magnitudes of the reflection coefficient $|S_{nn}|$ in that port and three transmission coefficients $|S_{mn}|$ ($m \neq n$) in other ports along with the phase characteristics of all these *S*-parameters $<S_{mn}$ (deg). For ANN computations, the magnitude and phase are converted to the real and imaginary parts of the *S*-parameters as follows:

$$\mathrm{Re}(S_{mn}) = |S_{mn}|\cos[\pi(<S_{mn})/180]; \quad \mathrm{Im}(S_{mn}) = |S_{mn}|\sin[\pi(<S_{mn})/180] \tag{2.12}$$

S-parameters of a waveguide structure depend on configuration of the imaged sample and distribution of material properties within this sample. Therefore, for each particular set of sample's characteristics, the simulator generates a set of *S*-parameters, so corresponding pairs of the simulator's input-output data can be used for training the ANN on the properties of the microwave system and subsequently (when measurement data is available) for reconstruction of characteristics of the imaged sample.

3. Microwave Imaging Problem – Reconstruction of a Spherical Inclusion

3.1 Statement of the Problem

In [12], [33], NDT functions were performed in a regular waveguide system. A technique for detection of a position and a size of a spherical inclusion within a dielectric sample was proposed in [33]. In that study, the electromagnetic wave propagates in the waveguide containing the tested sample holding a spherical inclusion inside (Figure 3.1). Characteristics of the wave reaching the output port depend on complex permittivity of both materials and their shapes. This presents an opportunity for the detection of the size and spatial positioning of the spherical inclusion inside of the tested sample.

However, microwave imaging capabilities of the waveguide system are rather limited. With only two ports available, it necessarily requires consideration of three spatial orientations of the sample; this implies that each orientation can detect characteristics of the sample only in one dimension [33]. Imaging in the waveguide also assumes that complex permittivity of the inclusion is known, but in many practical

16
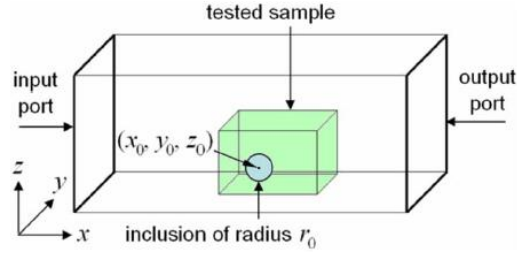
Figure 3.1. Waveguide structure for reconstruction of spatial coordinate and radius of the inclusion hidden inside a dielectric sample; one out of three required orientations of the sample [33].
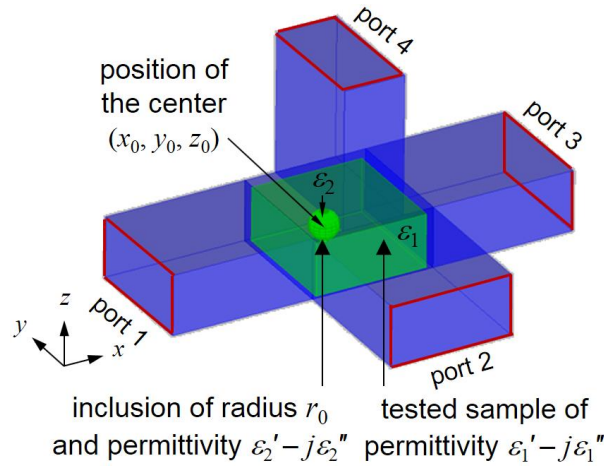
Figure 3.2. A Magic Tees Junction based system for reconstruction of spatial coordinate, radius, and dielectric properties of the inclusion inside a dielectric sample.

scenarios, this is not the case. It has later been suggested that imaging in closed systems can be made more precise by introducing additional ports (and thus by bringing in consideration additional waveguide modes and considering their response to the imaged sample). For example, in [34] a six-port device was successfully used to reconstruct 3-D profiles of complex permittivity of dielectric sample of rectangular and cylindrical shapes.

In this project, we develop the technique, which allows us to

(a) exclude the alternative spatial orientations, and

(b) determine dielectric properties of the hidden spherical inclusion.

The proposed technique relies on a four-port waveguide system. In contrast to a complicated artificially constructed structure in [34], the system considered in this project corresponds to a standard microwave component – a combination of four waveguides known as a Magic Tees Junction. In comparison with the system in Figure 3.1 [33], here the tested sample with a hidden inclusion faces the waves from two other ports propagating in the direction of the y- and z-axes. The records of responses of the fields in all four ports (i.e., the elements of the full matrix of S-parameters) are hypothesized to be sufficient for implementation of functions (a) and (b). The four-port Magic Tees Junction system containing the imaged sample is shown in Figure 3.2.

Similar to the previous studies [33]-[34], all electromagnetic processes in the considered closed system containing the imaged sample are simulated with the use of the 3D FDTD method. The model reproduces the four-port waveguide system, the tested sample (with complex permittivity ε_1) in the center of the junction, and a spherical inclusion of radius r_0 and complex permittivity ε_2 that is located in an arbitrary position within the tested sample. This model computes frequency characteristics of the real and imaginary parts of all S-parameters (2.12). Input data and output results of the FDTD model form the output and the input of the ANN. Multiple simulations performed for random values of the reconstructed parameters (taken in certain intervals) produce a database for training and testing the ANN. When the network is sufficiently well trained, it is given the experimental set of S-parameters corresponding to the unknown coordinates of the center of the inclusion $(x_0, y_0, z_0,)$, it radius $(r_0,)$ as well as its dielectric constant ε' and the loss factor ε''; the ANN then produces the reconstructed values of all these parameters.

3.2 ANN Solution of the Problem

To accomplish our goals, we came up with the ANN architecture show in Figure 3.3. The input parameters of the network consist of the real and imaginary parts of the S-parameters for three distinct frequencies. The output layer consists of geometrical and material parameters of the hidden spherical inclusion.
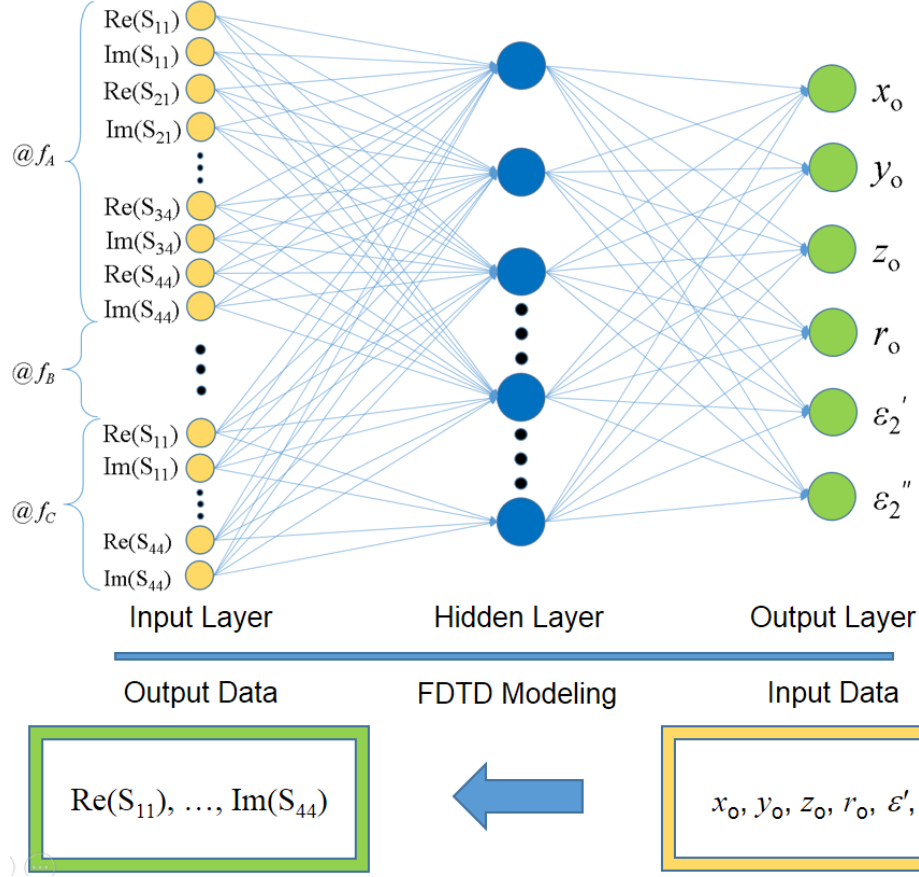
Figure 3.3 An ANN developed for a multiport waveguide system and the process of FDTD database generation.

It is worth mentioning that in modeling, we go in the opposite direction - as illustrated in Figure 3.3: parameters of the inclusion are the input parameters, and the *S*-parameters are in the output of the model. Here, we use the input/output modeling data for training the network and perform the neural network inversion.

For the training with *P* training points, the first step is to separate and create the set of input and output pairs for training $(\boldsymbol{f_1})$ and testing $(\boldsymbol{f_2})$. The column vector inputs $(\mathbf{X}_1, \ldots, \mathbf{X}_i)$, where *i* is the column number of training points. Training points are gathered from a database (created by the FDTD simulator, *QuickWave*) where each column vector consists of a real and a complex imaginary part in the form:

$$\boldsymbol{X_i} = [\, \mathrm{Re}(|S_{11}|) \quad \mathrm{Im}(|S_{11}|) \quad \ldots \quad \mathrm{Re}(|S_{4n}|) \quad \mathrm{Im}(|S_{4n}|) \,]. \tag{3.1}$$

where n is the port number. These input column vectors are paired with output column vectors $(\mathbf{Y}_1, …, \mathbf{Y}_n)$ consisting of known position and size parameters along with dielectric properties of the material of the spherical inclusion. The output column vectors are represented by:

$$Y_i = [x_0 \quad y_0 \quad z_0 \quad r_0 \quad \varepsilon_2' \quad \varepsilon_2''] \tag{3.2}$$

The network follows the principles of a radial basis function (RBF) neural network [37] that consists of a single hidden layer of neurons, where each neuron is comprised of an activation function multiplied by either a weight vectors or weight matrix. The RBF ANN is represented by $\phi(\mathbf{X}^{(1)})\mathbf{W}$, where $\mathbf{W}$ is the vector of weights, $\mathbf{X}^{(m)}$ indicates that the input vector consists of either training points (1) or testing points (2), and $\boldsymbol{\phi}(*)$ here is the activation function as the global Euclidean cubic function:

$$\boldsymbol{\phi}_l(X) = \|X_i - c_l\|^3, \tag{3.3}$$

where c_l is the center of $\boldsymbol{\phi}_l$, $l = 1, …, N_c$, and N_c is the number of centers in the training points.

The inputs are run through this network and then the least square error function is employed in the form:

$$\mathbf{E}(\mathbf{W}) = \frac{1}{2}\|\mathbf{Y}^{(1)} - \phi(\mathbf{X}^{(1)})\mathbf{W}\|_2^2 = \frac{1}{2}(\mathbf{Y}^{(1)} - \phi(\mathbf{X}^{(1)})\mathbf{W})^T(\mathbf{Y}^{(1)} - \phi(\mathbf{X}^{(1)})\mathbf{W}) \tag{3.4}$$

where $\mathbf{E}(\mathbf{W})$ is the error.

Solving the function directly by differentiating {3.3} with respect to $\mathbf{W}$ provides the least squares weights ($\hat{\mathbf{W}}$) as follows,

$$\mathbf{E}'(\mathbf{W}) = \left(\phi(\mathbf{X}^{(1)})\right)^T \left(\mathbf{Y}^{(1)} - \phi(\mathbf{X}^{(1)})\mathbf{W}\right) = \mathbf{0},$$

$$\left(\phi(\mathbf{X}^{(1)})\right)^T \mathbf{Y}^{(1)} = \left(\phi(\mathbf{X}^{(1)})\right)^T \phi(\mathbf{X}^{(1)})\mathbf{W},$$

$$\hat{W} = (\phi_1^T\phi_1)^{-1}\phi_1^T\mathbf{Y}^{(1)}, \tag{3.5}$$

where

$$\phi_1 = \boldsymbol{\phi}(\mathbf{X}^{(1)}). \tag{3.6}$$

The matrix $\phi_1^T\phi_1$ is inverted using singular value decomposition. If not all of the singular values are used, regularization is invoked for the values that are too close to zero [37].
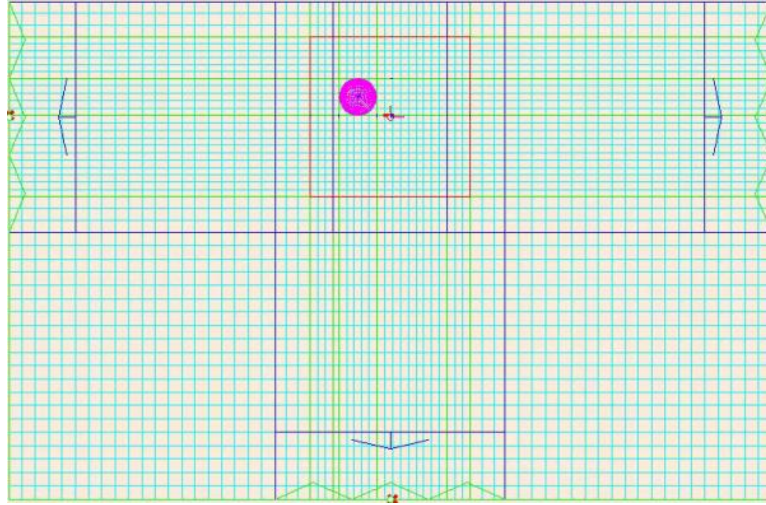
(a)
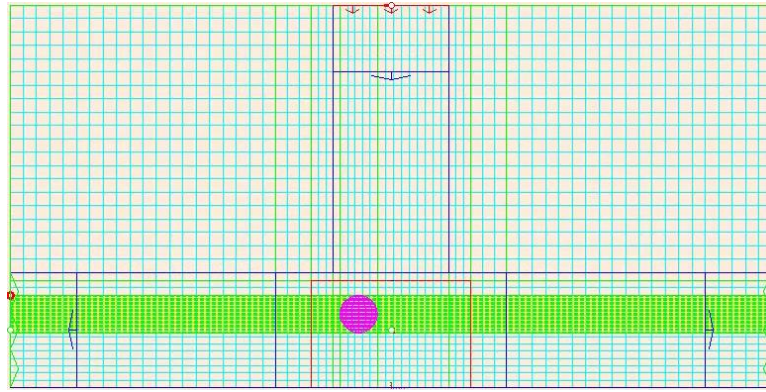
(b)

Figure 3.4. FDTD discretization of the Magic Tees Junction with the imaged sample viewed from above

(the *xy*-plane) (a) and from the side (the *xz*-plane) (b).

Once $\hat{W}$ has been calculated, the training process with the P training points is complete.

For the cross validation with Q points, the ANN is trained using various center vectors (c_l) then evaluated using a set of testing data pairs f_2 (see (2.9)). The c_l that produces the lowest error is chosen as the optimal c_l and the training is considered complete. With the cross validation complete the ANN can be used to precisely approximate the output parameters based on any given *S*-parameter inputs from the FDTD-generated database.
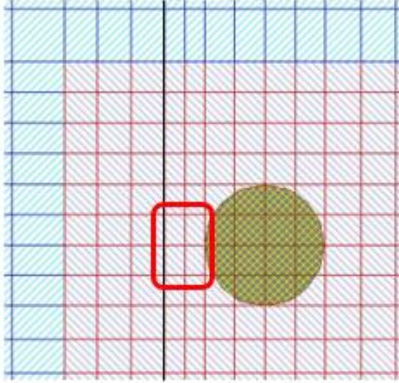
Figure 3.5 Close up of the vertical waveguide's boundary (black line) in the horizontal (*xy*-) plane.
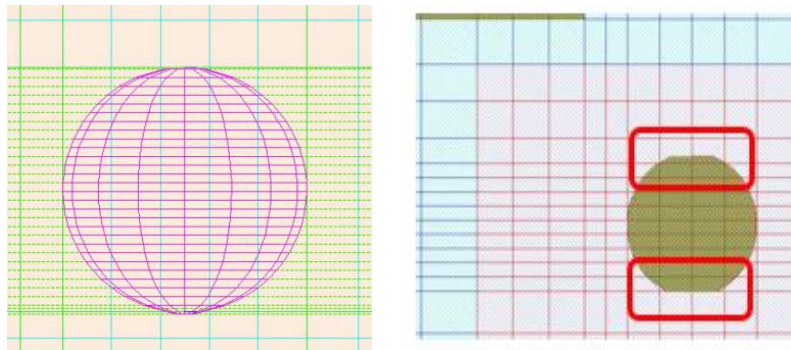
Figure 3.6. FDTD mesh around the spherical inclusion within the sample in the *xz*-plane: case of precise

approximation of the sphere (a) and the sphere with tiny portions on the top and on the bottom removed (b).

3.3 Model of the Closed Multiport System

The FDTD model representing a particular multi-port waveguide system known as the Magic Tees Junction generates data for the neural network. The views of the model in two coordinate planes (as seen in *QuickWave Editor*) are presented in Figure 3.4. The UDO script, the core *QuickWave* code describing the microwave system for simulator as a fully parameterized model, is given in Appendix A.1.

The mesh visible in Figure 3.4 is clearly non-uniform: the FDTD cells are smaller within the tested sample and around the spherical inclusion. In the effort of improving quality of reconstruction, the FDTD

22

mesh was "optimized": it was constructed following the standard condition for the number of cells per the wavelength in the medium:

$$\Delta x \leq (0.05 \div 0.1)\lambda_m, \tag{3.7}$$

where λ_m is the wavelength in the medium given by the formula

$$\lambda_m = \frac{c}{f\sqrt{\varepsilon}} \tag{3.8}$$

where f is free-space frequency and ε is relative dielectric constant of the medium.

The development of the model had to overcome a critical issue very small FDTD cells emerging in automatic mesh generation. Such small cells may be due to closeness of the sphere to the boundary of the vertical waveguide (as shown in Figure 3.5) and due to highly accurate approximation of geometry of the top and the bottom of the sphere (Figure 3.6(a)). Both issues were resolved by adding special constraints in the mesh generator and by allowing tiny portions of the sphere to be cut out – as shown in Figure 3.6(b).

4. Numerical Analysis

In the process of constructing the neural network, we used results of numerical (FDTD) analysis to help clarify available options. We used the *QuickWave* model of the WR340 Magic Tees Junction containing the tested sample with its spherical inhomogeneity (Figures 3.2 and 3.4). The key goal of the direct modeling of this system was to see variations of S-parameters with particular changes of geometrical and material parameters of the inclusion. By assessing the level of sensitivity of S-parameters to those changes, one can judge on the potential role of corresponding numerical data in ANN inversion.

The contents of Table 4.1 show the real and imaginary parts of S_{mn} associated with particular sets of geometric and material parameters. The top left portion of the table is the base case with corresponding values for radius (r_0), position (x_0, y_0, z_0), and complex permittivity of the inclusion ($\varepsilon = 6.69 - i0.1896$ for ZrO_2 and $\varepsilon = 10.4 - i0.9$ for SiC). In the top right part, there are values of S-parameters associated with a change in material properties (from ZrO_2 to SiC). The bottom left portion of the table displays the S-parameters for a change in radius. Finally, in the bottom right, there are the values for a change in the position of the center of the sphere. It is seen that numerical values in different parts of Table 4.1 are of measurable difference, so they should be able to play a certain role in numerical inversion.
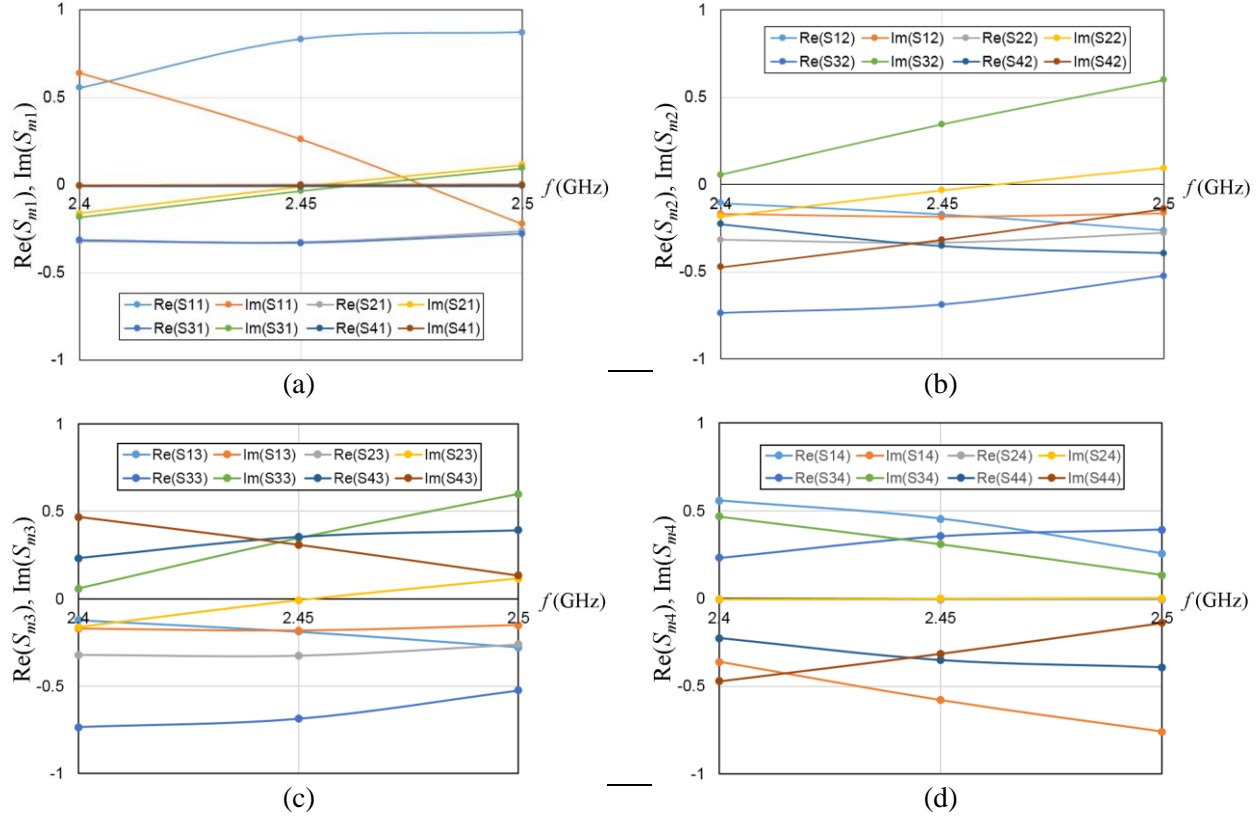
Figure 4.1. Frequency characteristics of real and imaginary parts of S-parameters computed at Port 1 (a), Port 2 (b), Port 3 (c), and Port 4 (d) for $r_0 = 4.75$mm; $x_0 = 15$mm, $y_0 = 10$mm, $z_0 = 5$mm; spherical inclusion: ZrO_2.

Table 4.1. Real and Imaginary Parts of Complex S-Parameters at 2.45 GHz for WR340 Magic Tess Containing the 60x60x40 mm Teflon Sample.

Port #	1	2	3	4
Re(S1n)	0.833277	-0.18836	-0.16984	0.45442
Im(S1n)	0.262434	-0.18171	-0.18496	-0.58039
Re(S2n)	-0.325956	-0.3259	-0.33045	-0.00625
Im(S2n)	-0.009914	-0.00978	-0.03314	-0.00059
Re(S3n)	-0.330469	-0.6872	-0.6872	0.354494
Im(S3n)	-0.033196	0.346533	0.346533	0.308611
Re(S4n)	-0.006242	0.354443	-0.35196	-0.35196
Im(S4n)	-0.000589	0.308587	-0.31504	-0.31505

$r_0 = 4.75$mm; $x_0 = 15$mm, $y_0 = 10$mm, $z_0 = 5$mm; ZrO_2

Port #	1	2	3	4
Re(S1n)	0.833277	-0.18836	-0.16984	0.45442
Im(S1n)	0.262434	-0.18171	-0.18496	-0.58039
Re(S2n)	-0.325956	-0.3259	-0.33045	-0.00625
Im(S2n)	-0.009914	-0.00978	-0.03314	-0.00059
Re(S3n)	-0.330469	-0.6872	-0.6872	0.354494
Im(S3n)	-0.033196	0.346533	0.346533	0.308611
Re(S4n)	-0.006242	0.354443	-0.35196	-0.35196
Im(S4n)	-0.000589	0.308587	-0.31504	-0.31505

$r_0 = 4.75$mm; $x_0 = 15$mm, $y_0 = 10$mm, $z_0 = 5$mm; SiC

Port #	1	2	3	4
Re(S1n)	0.833277	-0.18836	-0.16984	0.45442
Im(S1n)	0.262434	-0.18171	-0.18496	-0.58039
Re(S2n)	-0.325956	-0.3259	-0.33045	-0.00625
Im(S2n)	-0.009914	-0.00978	-0.03314	-0.00059
Re(S3n)	-0.330469	-0.6872	-0.6872	0.354494
Im(S3n)	-0.033196	0.346533	0.346533	0.308611
Re(S4n)	-0.006242	0.354443	-0.35196	-0.35196
Im(S4n)	-0.000589	0.308587	-0.31504	-0.31505

$r_0 = 7.14$mm; $x_0 = 15$mm, $y_0 = 10$mm, $z_0 = 5$mm; ZrO_2

Port #	1	2	3	4
Re(S1n)	0.833277	-0.18836	-0.16984	0.45442
Im(S1n)	0.262434	-0.18171	-0.18496	-0.58039
Re(S2n)	-0.325956	-0.3259	-0.33045	-0.00625
Im(S2n)	-0.009914	-0.00978	-0.03314	-0.00059
Re(S3n)	-0.330469	-0.6872	-0.6872	0.354494
Im(S3n)	-0.033196	0.346533	0.346533	0.308611
Re(S4n)	-0.006242	0.354443	-0.35196	-0.35196
Im(S4n)	-0.000589	0.308587	-0.31504	-0.31505

$r_0 = 4.75$mm; $x_0 = -20$mm, $y_0 = -20$mm, $z_0 = -10$mm; ZrO_2

We also wished to expand the amount of representative data to increase quality of imaging and a number of reconstructed parameters. To this end, values of S-parameters at multiple frequencies look attractive: in FDTD simulation, they are readily available (i.e., do not need to be separately computed). The ANN developed in this project intends to use the values of S-parameters at two additional frequencies – 2.4 and 2.5 GHz. From the typical frequency characteristics of $\mathrm{Re}(S_{mn})$ and $\mathrm{Im}(S_{mn})$ (Figure 4.1), one can see that the values of S-parameters are indeed frequency-dependent. This implies that the additional data at 2.4 and 2.5 GHz could bring additional information about the system to the neural network, which can be used for greater accuracy of reconstruction.

5. Implementation of the Algorithm

In terms of computational operation of the ANN technique outlined in previous section, the phase of data processing in the considered system of microwave imaging can be broken down into five major steps.

Following Figures 5.1 and 5.2, the operation starts from the development of an (accurate and adequate) FDTD model of the microwave system to be used in the experimental setup. In this project, such a model (built for *QuickWave*) represents the 4-port waveguide junction containing the tested sample (Figure 3.2). The ANN inversion backed by the FDTD data is implemented in a series of MATLAB scripts, which also control operation of *QuickWave*. Search intervals for the parameters to be reconstructed are specified in the MATLAB code (in `QWStarter` function). `QWStarter` also calls *QuickWave* to run multiple simulations of the model to generate *S*-parameters to be used for ANN training and testing. The code utilizes random values generated for the position, radius, and material parameters of the inclusion (and specified within the search intervals) to return corresponding *S*-parameters. Once *QuickWave* simulations are complete, the database (containing vectors of input/output pairs of FDTD data) is formed, and numbers of training and testing points are specified (function `MSplitter`). Next steps correspond to the ANN training and testing processes described in Section 2.3 (function `RBFrunner`). Computational results are
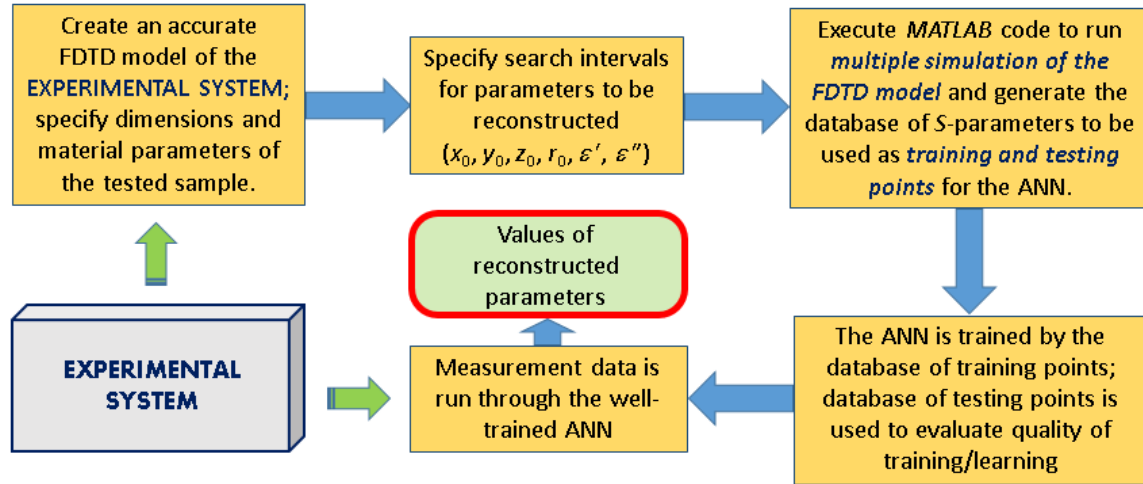
Figure 5.1 Flow chart of FDTD-backed ANN-based reconstruction of the position (x_0, y_0, z_0), radius (r_0), dielectric constant (ε') and the loss factor (ε'') of a spherical inclusion in the tested sample.
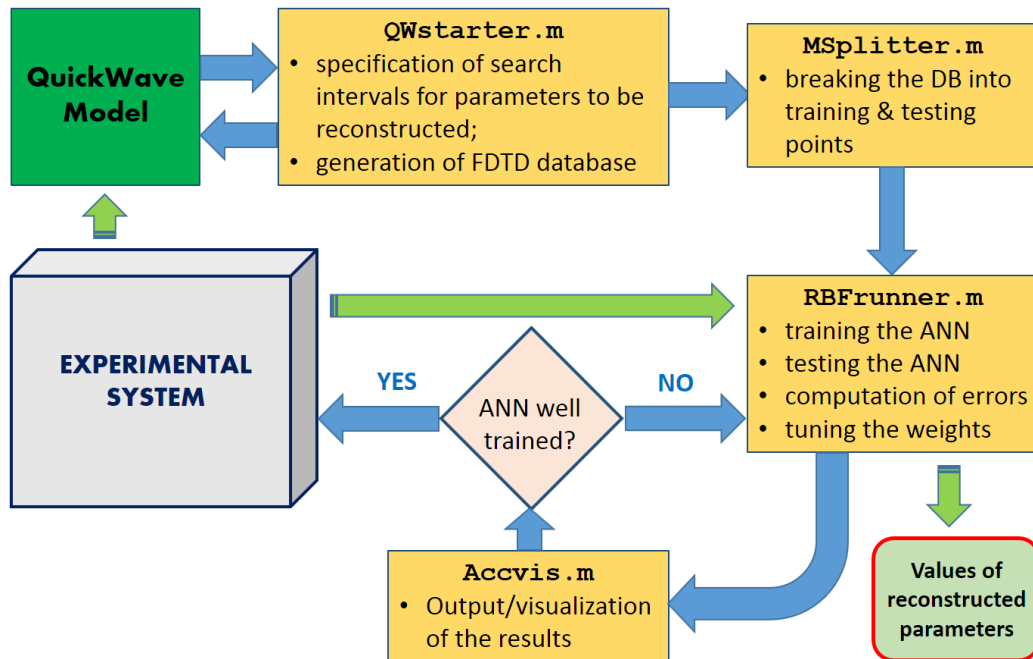
Figure 5.2 Flow chart of the computational procedure (with the name of the MATLAB functions) and its interaction with the experimental system and n FDTD model.

outputted and visualized (function `Accvis`). Once it is determined that the network is well trained, it can be used for imaging the spherical inclusion: data on a single measurement of *S*-parameters is run through

28

the network in the same manner as the testing point; yet, now the measured data represent the actual responses of the electromagnetic field to the tested sample with a spherical inclusion hidden inside it. The ANN procedure reconstructs then the values of x_0, y_0, z_0, r_0, ε' and ε'' corresponding to that inclusion.

While used in this project with the *QuickWave* model of the WR340 Magic Tees Junction containing a rectangular Teflon block with a spherical inhomogeneity, the developed MATLAB code can be easily adapted to another FDTD model (built for alternative microwave system, different shape of the sample, alternative parameters of reconstruction and their number, another FDTD simulator, etc.). It is therefore fully applicable to implementations of microwave imaging technology in other closed systems.

6. Microwave Imaging in Computational Results

6.1. Parameters of Reconstruction

Performance of the ANN inversion procedure is illustrated by its operation with a dielectric and metal sphere hidden in a rectangular Teflon sample inside a Magic Tees Junction. First, the procedure was run to reconstruct four geometrical parameters – the coordinates (x_0, y_0, z_0) and the radius (r_0) of the inclusion whose material parameters (dielectric constant ε' and the loss factor ε'') were supposed to be known. This set of parameters was reconstructed in the earlier study [33], however, the technique presented in that paper required measurement of S-parameters for three different spatial orientations of the sample. In the ANN procedure developed in the present report, the rotation is not required and all the parameters are reconstructed from a single measurement.

As the quality/accuracy of reconstruction with the new ANN procedure is expected to be improved, in the second test, the procedure was used to evaluate its computational resources in reconstructing of six parameters of the inclusion – the same geometrical characteristics plus two material parameters (x_0, y_0, z_0, r_0, ε' and ε'').
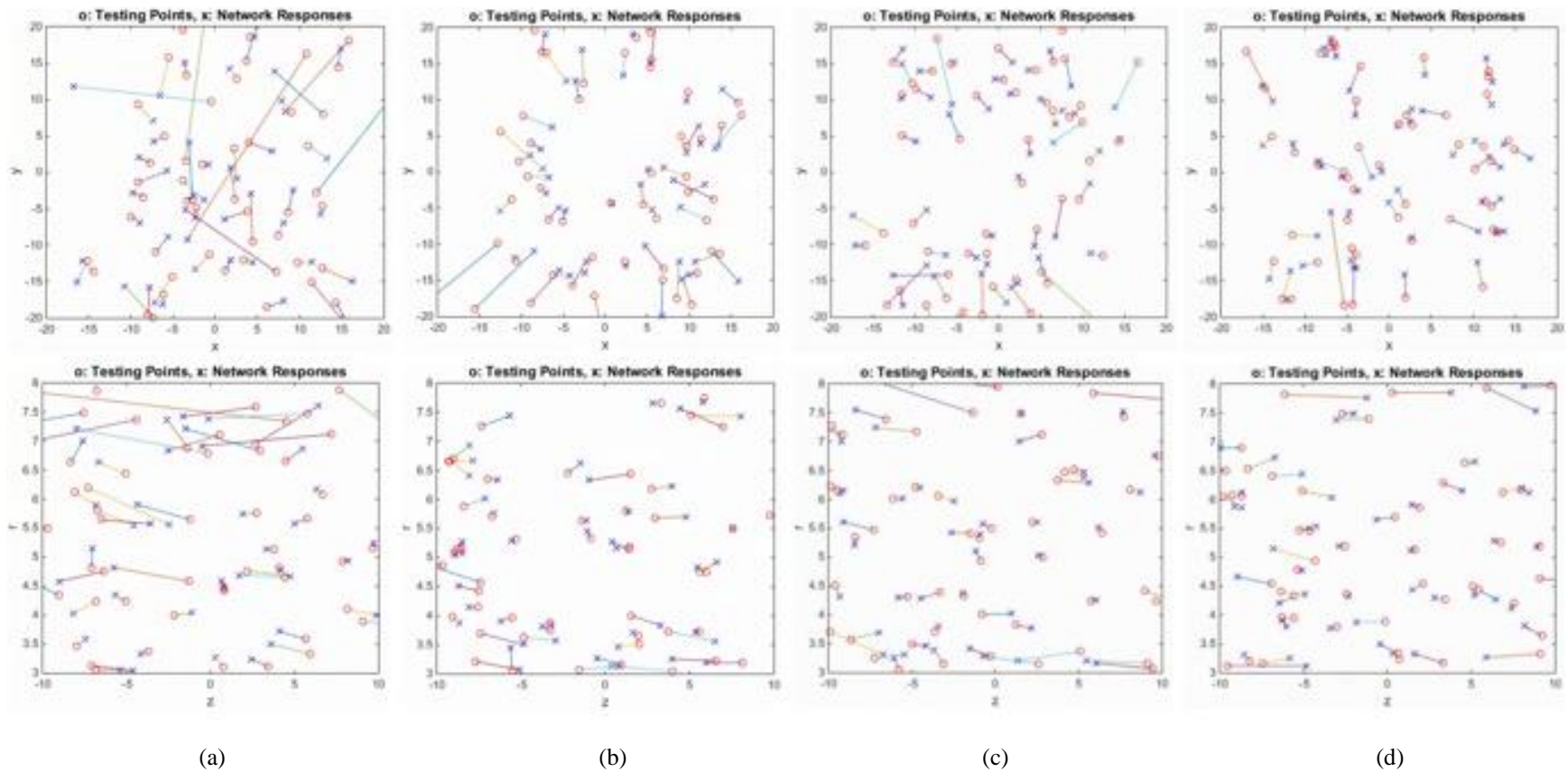
(a)　　　　　　　　　　(b)　　　　　　　　　　(c)　　　　　　　　　　(d)

Figure 6.1 Reconstruction of four geometrical parameters (x_0, y_0, z_0, r_0) for the spherical inclusion made of ZrO_2 with 500 (a), 1000 (b), 1500 (c), and 2000 (d) training points in the intervals: $-20 \leq x \leq 20$ mm; $-20 \leq y \leq 20$ mm; $-10 \leq z \leq 10$ mm; $3 \leq r \leq 8$ mm; number of testing points: 50.
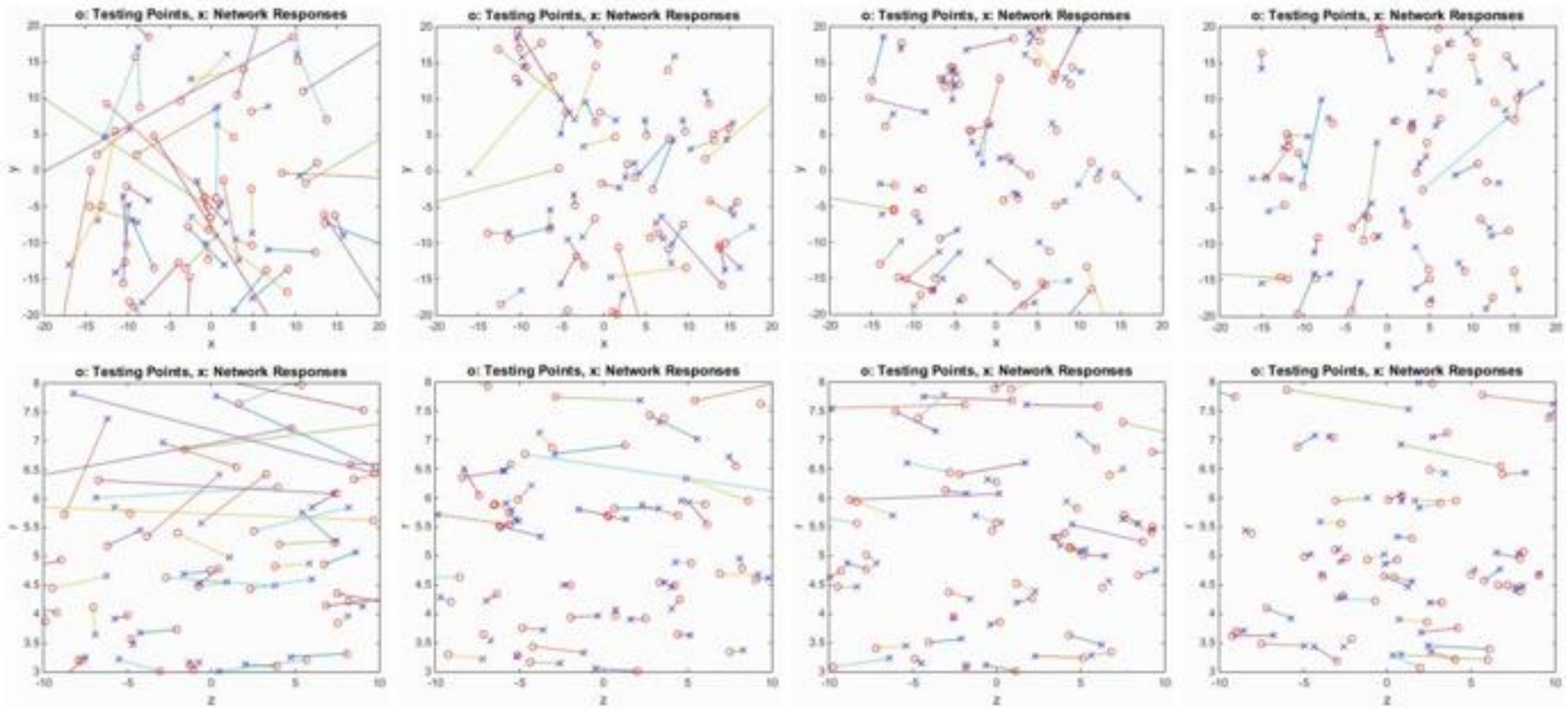
Figure 6.2 Reconstruction of four geometrical parameters (x_0, y_0, z_0, r_0) for the spherical inclusion made of SiC with 250 (a), 500 (b), 750 (c), and 1000 (d) training points in the intervals: $-20 \leq x \leq 20$ mm; $-20 \leq y \leq 20$ mm; $-10 \leq z \leq 10$ mm; $3 \leq r \leq 8$ mm; number of testing points: 50.

(e)   (f)   (g)   (h)
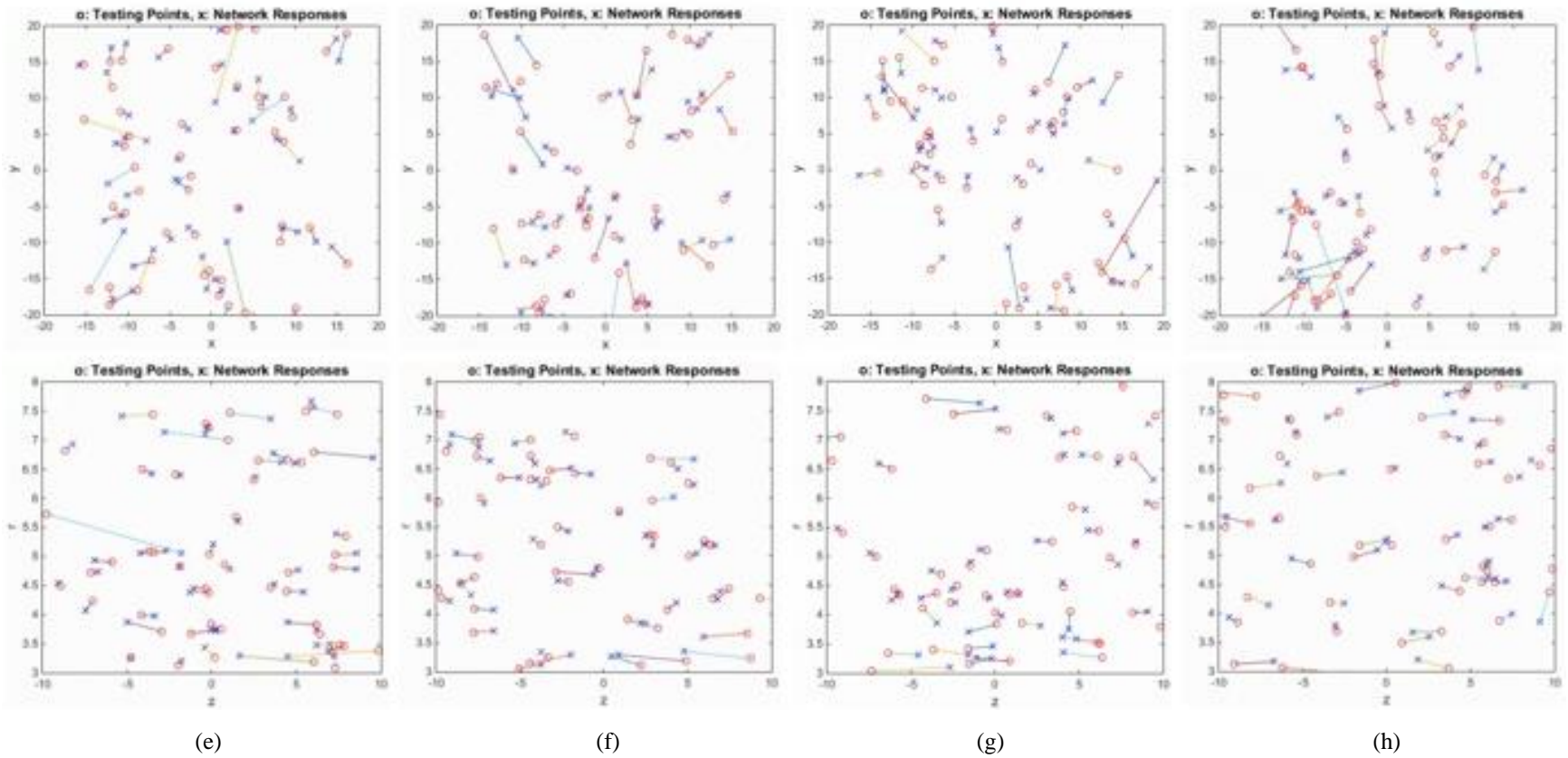
Figure 6.2 (*cont'd*). Reconstruction of four geometrical parameters (x_0, y_0, z_0, r_0) for the spherical inclusion made of SiC with 1250 (a), 1500 (b), 1750 (c), and 1000 (d) training points in the intervals: $-20 \le x \le 20$ mm; $-20 \le y \le 20$ mm; $-10 \le z \le 10$ mm; $3 \le r \le 8$ mm; number of testing points: 50.
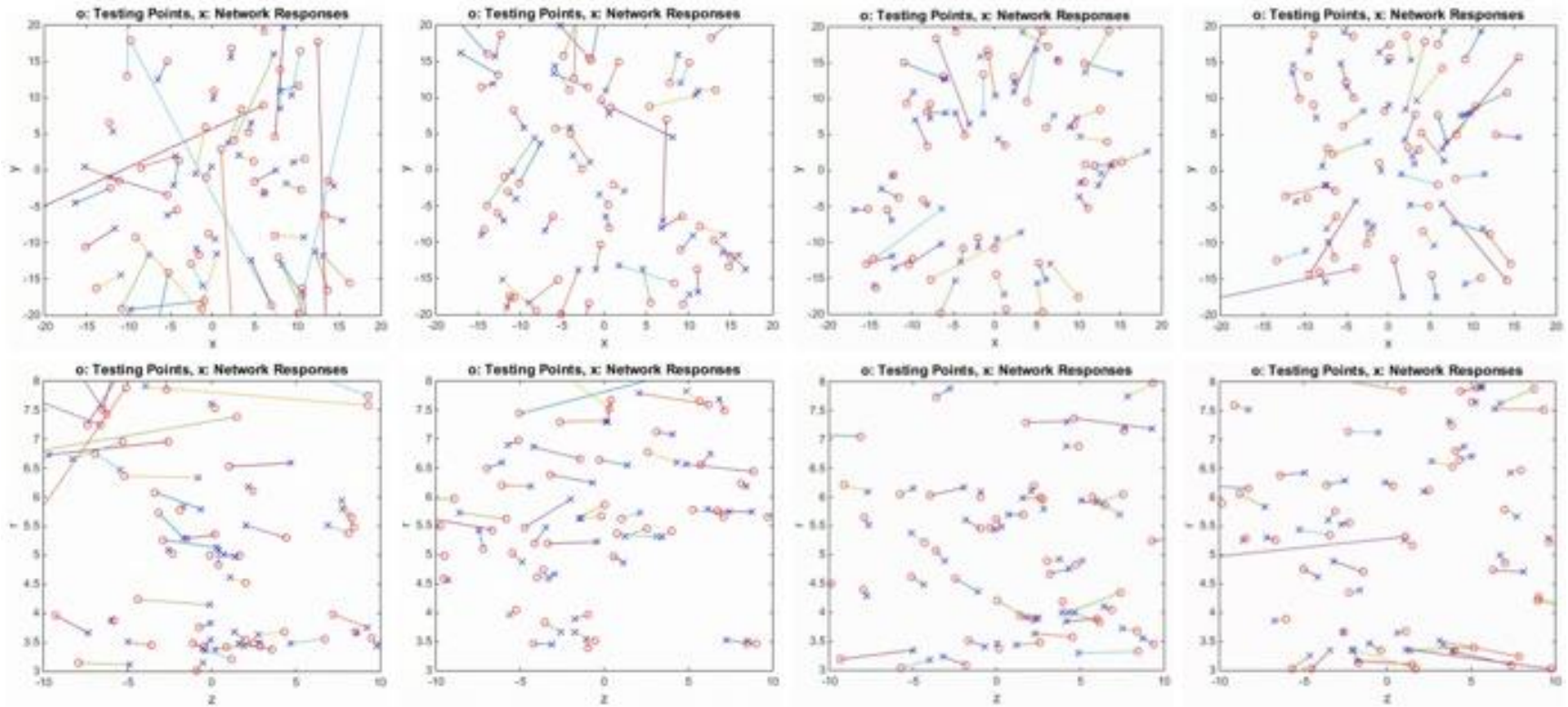
Figure 6.3. Reconstruction of four geometrical parameters (x_0, y_0, z_0, r_0) for the spherical inclusion made of metal with 500 (a), 1000 (b), 1500 (c), and 2000 (d) training points in the intervals: $-20 \leq x \leq 20$ mm; $-20 \leq y \leq 20$ mm; $-10 \leq z \leq 10$ mm; $3 \leq r \leq 8$ mm; number of testing points: 50.
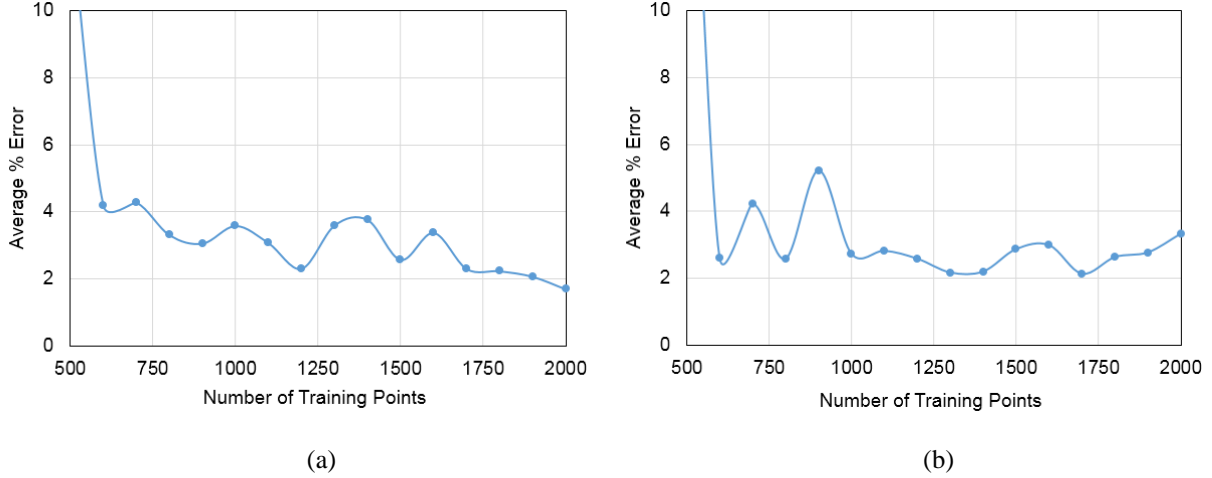
Figure 6.4. Convergence of computational procedure for the sphere made of ZrO_2 (a) and SiC (b).

In both reconstructions, computations were performed for the following geometrical and material parameters:

o WR340 Magic Tees Junction (cross-section 86×43 mm)

o Rectangular block ($60 \times 60 \times 40$ mm)

o Teflon $\varepsilon_1 = 2.04 - i0.004$

o Silicon Carbide (SiC): $\varepsilon_2 = 10.4 - i0.9$

o Zirconia (ZrO_2): $\varepsilon_2 = 6.69 - i0.1$

The reconstructed parameters were sought within the following integrals: $-20 \le x \le 20$ mm, $-20 \le y \le 20$ mm, $-10 \le z \le 10$ mm, $3 \le r \le 8$ mm, $7 \le \varepsilon' \le 13$; $0.5 \le \varepsilon'' \le 1.5$.

For each parameter, the error was calculated using a formula that takes into account the bounds of the randomly generated values of the input parameters:

$$Percent\ Error = \frac{|P_a - P_r|}{CI} 100 , \qquad (6.1)$$

where P_a and P_r are the actual and reconstructed values of the parameters and CI stands for a "conditional interval" which is specified in accordance with physical constraints for a particular parameter in the considered scenario. For the coordinates of the center of the inclusion (x_0, y_0, z_0), we define CI as the physical dimensions of the sample, i.e., $CI_x = CI_y = 60$ mm, and $CI_z = 40$ mm. For the radius (r_0), the CI is

35

Table 6.1 Examples of Individual Four Parameter Reconstructions for ZrO$_2$ and SiC

Zirconia ($\varepsilon_2 = 6.69 - i0.1896$)

	Paramters:	x0 (mm)	y0 (mm)	z0 (mm)	r0 (mm)
	Actual:	-12.23	-17.70	5.31	4.35
Test 1	Reconstructed:	-11.63	-17.49	5.09	4.49
	% error:	1.01	0.35	0.56	2.94
	Paramters:	x0 (mm)	y0 (mm)	z0 (mm)	r0 (mm)
	Actual:	-5.04	-4.91	2.49	7.92
Test 2	Reconstructed:	-4.95	-6.63	0.27	7.86
	% error:	0.16	2.87	5.53	1.18
	Paramters:	x0 (mm)	y0 (mm)	z0 (mm)	r0 (mm)
	Actual:	7.60	2.42	0.37	3.32
Test 3	Reconstructed:	8.38	3.93	0.73	3.24
	% error:	1.30	2.52	0.89	1.67
	Paramters:	x0 (mm)	y0 (mm)	z0 (mm)	r0 (mm)
	Actual:	-4.15	-13.45	-1.63	7.47
Test 4	Reconstructed:	-4.30	-18.28	-2.68	7.49
	% error:	0.24	8.05	2.63	0.53
	Paramters:	x0 (mm)	y0 (mm)	z0 (mm)	r0 (mm)
	Actual:	-4.55	-12.14	-4.28	5.53
Test 5	Reconstructed:	-3.96	-11.37	-4.61	5.45
	% error:	0.98	1.27	0.82	1.46

Silicon Carbide ($\varepsilon_2 = 10.4 - i0.9$)

	Paramters:	x0 (mm)	y0 (mm)	z0 (mm)	r0 (mm)
	Actual:	-10.57	-14.00	3.61	7.80
Test 1	Reconstructed:	-4.20	-11.75	4.81	7.89
	% error:	10.61	3.74	2.98	1.94
	Paramters:	x0 (mm)	y0 (mm)	z0 (mm)	r0 (mm)
	Actual:	16.06	-2.69	3.28	4.48
Test 2	Reconstructed:	12.79	-3.05	4.35	4.39
	% error:	5.45	0.59	2.67	1.65
	Paramters:	x0 (mm)	y0 (mm)	z0 (mm)	r0 (mm)
	Actual:	-0.36	18.95	-7.03	4.15
Test 3	Reconstructed:	-0.87	13.09	-8.28	4.29
	% error:	0.84	9.76	3.13	2.79
	Paramters:	x0 (mm)	y0 (mm)	z0 (mm)	r0 (mm)
	Actual:	-2.59	-8.86	-10.27	5.72
Test 4	Reconstructed:	-2.07	-8.19	-8.12	5.55
	% error:	0.86	1.12	5.37	3.32
	Paramters:	x0 (mm)	y0 (mm)	z0 (mm)	r0 (mm)
	Actual:	11.47	-13.66	-2.62	6.44
Test 5	Reconstructed:	12.82	-11.20	-4.15	6.38
	% error:	2.25	4.11	3.84	1.34

Table 6.2. Average % Error in Reconstruction of Four Geometrical Parameters*)

	Material	x_0	y_0	z_0	r_0	Overall
Dielectric (mineral)	Zirconium dioxide (ZrO$_2$) $\varepsilon = 6.69 - i0.1896$	1.10	2.18	2.13	1.35	*1.7*
Dielectric (ceramics)	Silicon carbide (SiC) $\varepsilon = 10.4 - i0.9$	3.84	4.72	3.06	1.66	*3.3*
Metal	Stainless steel $\sigma = 10^7$ (S/m)	12.76	7.3	7.21	2.82	*7.5*

*) ANN training points: 2000; average over 15 testing points

defined by the interval in which variation of the size of the sphere is assumed to be possible, i.e., $CI_r = 5$ mm. Similar definitions are applied for the "conditional interval" for the material parameters (ε' and ε''): $CI_{\varepsilon'} = 6$ and $CI_{\varepsilon''} = 1$.
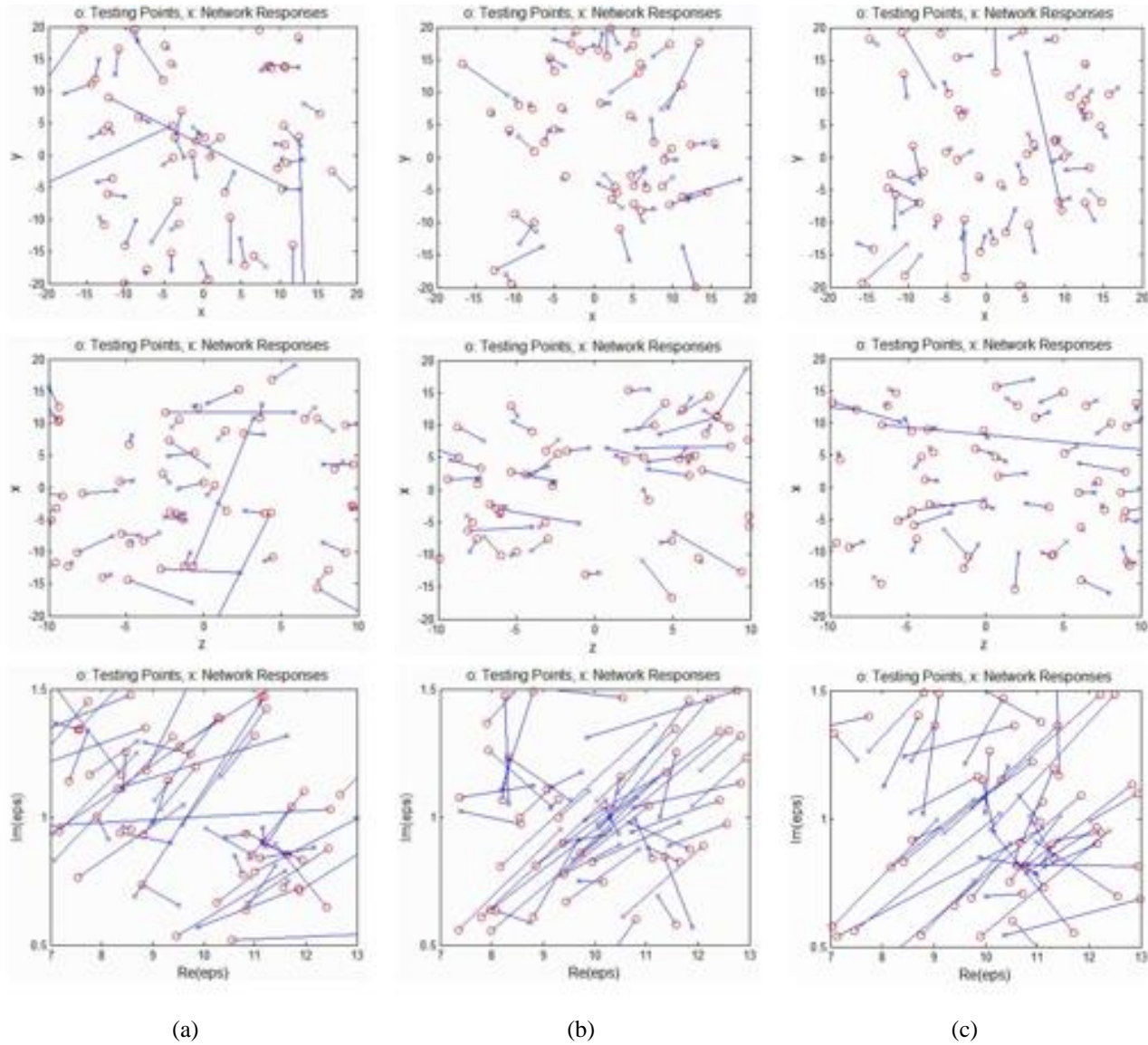
(a)   (b)   (c)

Figure 6.5. Reconstruction of six geometrical (x_0, y_0, z_0, r_0) and material (ε' and ε'') parameters for the spherical inclusion with 1000 (a), 1500 (b), and 2000 (c) training points in the intervals: $-20 \leq x \leq 20$ mm, $-20 \leq y \leq 20$ mm, $-10 \leq z \leq 10$ mm, $3 \leq r \leq 8$ mm, $7 \leq \varepsilon' \leq 13$, and $0.5 \leq \varepsilon'' \leq 1.5$; number of testing points: 50.

37

6.2. Reconstruction of Four Geometrical Parameters

A series of special diagrams showing the quality of reconstruction of the coordinates and the radius of a spherical inclusion in the Teflon block insides the WR340 Magic Tees Junction is shown in Figures 6.1-6.3 for zirconia, silicon carbide, and metal, respectively. The tested points are shown by circles, and the points reconstructed by the network by crosses. The disagreement between the two positions is highlighted by a straight line between them. It is seen that for all materials of the inclusion the accuracy of reconstruction improves with the number of training points, and the performance is better for ZrO_2 and SiC than for metal. In Figure 6.4, the average percent error is shown as the function of number of training points. One can see an excellent convergence: the error drops below 4% when the number of training points is larger than 500. Details of reconstruction of five sets of geometrical parameters for the ZrO_2 and SiC spheres are given in Table 6.1. The five points were randomly taken from the last 15 points in the testing set. While many geometrical parameters are reconstructed with very high accuracy, there are some individual disagreements by about 10%. However, the average percent errors in reconstruction, as seen from Table 6.2, is high: computed for the 15 points from the testing set, the errors are 1.7% and 3.3% for dielectric inclusions and 7.5% for a metal sphere.

6.3. Reconstruction of Six Geometrical and Material Parameters

The developed computational procedure was also used in reconstruction of both geometrical and material parameters of a spherical inclusion. The diagrams showing the quality of reconstruction are presented in Figure 6.5. It turned out that the errors in finding the coordinates and radius are comparable with the accuracy of the four-parameter reconstructions (Section 6.2), but dielectric constant and the loss factor are determined with notable diversions from the actual values. The average percent error in reconstruction all fix parameters stands on the level of about 10% for the number of training points exceeding 600 (Figure

38
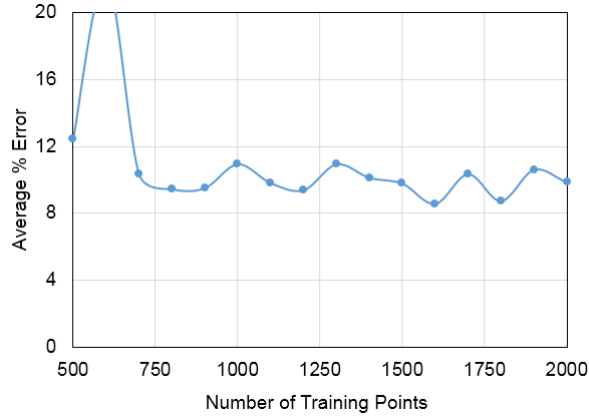
Figure 6.6. Convergence of computational procedure for six parameter reconstruction.

Table 6.3. Examples of Individual Six Parameter Reconstructions

		x0 (mm)	y0 (mm)	z0 (mm)	r0 (mm)	eps'	eps"
	Paramters:						
	Actual:	9.76	-8.18	-6.64	7.98	10.47	0.75
Test 1	Reconstructed:	6.40	16.18	9.87	7.70	12.51	1.27
	% error:	5.59	40.60	41.30	5.48	34.13	52.05
	Paramters:	x0 (mm)	y0 (mm)	z0 (mm)	r0 (mm)	eps'	eps"
	Actual:	12.63	14.34	-6.28	4.54	11.27	0.90
Test 2	Reconstructed:	12.73	14.25	-6.12	4.57	11.08	0.82
	% error:	0.17	0.15	0.40	0.57	3.25	8.26
	Paramters:	x0 (mm)	y0 (mm)	z0 (mm)	r0 (mm)	eps'	eps"
	Actual:	-3.10	6.46	4.10	5.44	11.12	0.73
Test 3	Reconstructed:	-2.60	7.09	2.59	5.46	10.91	0.78
	% error:	0.83	1.05	3.78	0.32	3.51	5.19
	Paramters:	x0 (mm)	y0 (mm)	z0 (mm)	r0 (mm)	eps'	eps"
	Actual:	-0.83	-3.11	6.06	4.07	10.66	0.90
Test 4	Reconstructed:	-0.76	-3.28	7.04	4.16	10.54	0.82
	% error:	0.11	0.29	2.45	1.83	1.93	8.72
	Paramters:	x0 (mm)	y0 (mm)	z0 (mm)	r0 (mm)	eps'	eps"
	Actual:	-3.65	15.32	-4.66	7.52	8.75	0.55
Test 5	Reconstructed:	-1.86	15.98	0.63	7.30	9.77	0.74
	% error:	2.99	1.10	13.20	4.48	16.99	19.29

Table 6.4. Average % Error in Reconstruction of Six Parameters*)

x_0	y_0	z_0	r_0	ε'	ε''	Overall
2.0	6.9	5.0	3.1	21.2	21.0	*9.87*

*) ANN training points: 2000; average over 15 testing points

6.6.) Details of reconstruction of five testing points are exemplified in Table 6.3. On the basis of 15 testing points (chosen, similarly to the four-parameter reconstruction, as the last points in the set of 50 testing points) it appears that the coordinates of the center of the spherical inclusion are determined with the average errors between 2.0 % and 6.9 %, but dielectric constant and the loss factor are reconstructed with approximately 21% error. This means that, while the ANN technique developed in this project has a clear potential for full reconstruction of a spherical inclusion, insufficient accuracy in determination of material parameters should be addressed in the future developments of the technique and its implementation.

7. Prospective Experimental Implementation

The ANN inversion procedure developed in this project demonstrates its reliability and robustness, and the results of accurate reconstruction of geometrical parameters of a dielectric spherical inclusion hidden in the Teflon sample suggest that the proposed technique may show satisfactory level of accuracy in its implementation with corresponding experimental system. It is therefore apparent that this project has created a solid theoretical background for the experimental program studying the resources and capabilities of a multiport closed system for microwave imaging. The initial steps of such experimental program are outlined in this sub-section.

The conceptual parts of the proposed experimental setup are illustrated in Figure 7.1. A standard Magic Tees Junction appears to be convenient and easily producible waveguide component which can become a basic element of the closed experimental system of microwave imaging. The WR340 Magic Tees Junction and corresponding waveguide-to-coax adaptors are currently being produced by Vector Tele Ltd., Melbourne, Australia. The experimental program is scheduled for Summer 2017 at the Computational Electromagnetics Research Laboratory, McMaster University, Hamilton, ON, Canada. This laboratory is in a possession of a four-input Vector Network Analyzer (Advantest R3770) required for simultaneous measurement of all S-parameters in all ports.
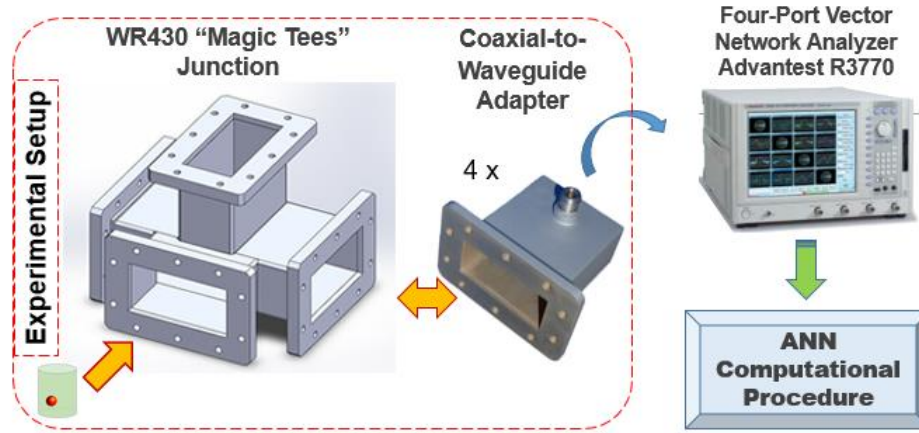
Figure 7.1 Elements of the experimental implementation.
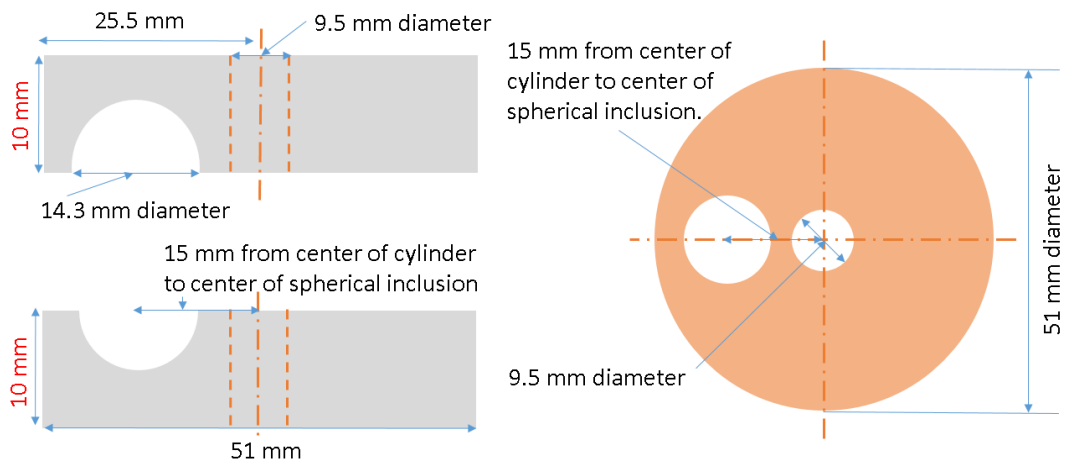
Figure 7.2. Internal structure of the tested Teflon sample.
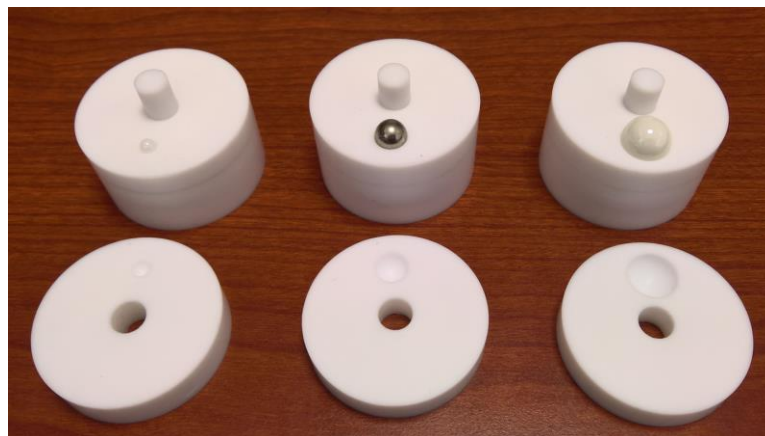
Figure 7.3. Manufactured test samples: a Teflon cylinder with a hidden spherical (dielectric or metal) inclusion.

The internal structure of the sample designed for the experiment is illustrated by Figure 7.2. The cylindrical Teflon sample of 40 mm height consists of the 20 mm base and two disks that have semi-spherical pits cut in them to house a spherical inclusion. In three different samples, the pits are of 4.75 mm, 7.5 mm and 14.3 mm diameter; they can be filled by either dielectric (ZrO_2 or SiC), or metal spheres. A Teflon rod is used to hold the pieces in place. In Figure 7.2, one can see the set of produced test samples.

8. Conclusion

The material presented above makes it evident that all the objectives of the project have been successfully achieved. The developed ANN inversion procedure was used with an FDTD model of a four-port closed system, the standard (WR340) Magic Tees Junction, and processed complex values of the full matrix of S-parameters. It was shown that the procedure was capable of precise reconstructing the spatial coordinates of the center and the radius of a spherical inhomogeneity inside the Teflon sample placed inside the junction. Both dielectric and metal inhomogeneities were considered; the overall average errors in reconstruction were 1.7-3.3 % and 7.5 %, respectively. In the latter case, the procedure was also able to determine material parameters (dielectric constant and the loss factor) of the sphere, but the accuracy of this reconstruction was higher – on the level of 10%.

While the earlier reported technique of ANN-backed reconstruction of the geometrical parameters of a spherical inclusion required three spatial orientations of the tested sample, in this project, all the results were obtained for a single position. Therefore, for full reconstruction of the spherical inclusion, the developed computational technique requires a single simultaneous measurement of S-parameters in all ports of the system.

The ANN procedure is computationally expensive at the stage preceding the actual measurement (because it requires generation of large database of the input/output data of the related FDTD model), however, once the database is created (i.e., once the ANN is trained), the CPU required for the reconstruction is measured in seconds.

The output of this project can be considered a solid theoretical background of the upcoming experimental program. The procedure can be easily adapted to another FDTD model (built for an alternative microwave system, different shape of the sample, alternative parameters of reconstruction and their number, another FDTD simulator, etc.). It is therefore fully applicable to implementations of microwave imaging technology in other closed systems. The immediate future work in further development of the procedure will be focused on the improvement of accuracy in reconstruction of material parameters of the spherical inclusion.

Appendix

A.1 *QuickWave* UDO Scripts (**.udo*)

```
comment = "Double T junction";
bitmap = "nobitmap.bmp";

PAR( "Object name", oname, "doublet1" );

PAR( "Waveguide wide wall", Ww, 86.36);
PAR( "Waveguide narrow wall", Wn, 43.18);
PAR( "Waveguide tail lengthl", Wt, 100);

# Basic mesh cell sizes
PAR("Maximum cell size in x-dir", cx, 5);
PAR("Maximum cell size in y-dir", cy, 5);
PAR("Maximum cell size in z-dir", cz, 5);

# Mesh cell sizes in the sample
PAR("cell size in sample in x-dir", smeshx, 3);
PAR("cell size in sample in y-dir", smeshy, 3);
PAR("cell size in sample in z-dir", smeshz, 3);

ENDHEADER;

OPENOBJECT( oname );

# GEOMETRICAL ELEMENTS

CALL("basic/cubo.udo", mid, Ww, Ww, Wn, air, E, 0, x, y, z, 11);
CALL("basic/cubo.udo", wgd1, Ww, Wt, Wn, air, E, 0, x, y-Ww/2-Wt/2, z, 11);
CALL("basic/cubo.udo", wgd2, Wt, Ww, Wn, air, E, 0, x+Ww/2+Wt/2, y, z, 11);
CALL("basic/cubo.udo", wgd3, Wt, Ww, Wn, air, E, 0, x-Ww/2-Wt/2, y, z, 11);
CALL("basic/cubo.udo", wgd4, Wn, Ww, Wt, air, E, 0, x, y, z+Wn, 11);
```

```
# SAMPLE

# Open the parameters of sphere
OPENF( "params.dat" );
x0 = READF;
y0 = READF;
z0 = READF;
r0 = READF;
Epsilon1 = READF;
Epsilon2 = READF;
bl = READF;
bw = READF;
bh = READF;

# Sample: Teflon
Eps1 = 2.04;
Sig1 = 0.00054;

INSERTMEDIUM(smed, ISOTROPIC) ;
MEDIUMPAR( smed, Eps1, 1, Sig1, 0, Eps1, 1, Sig1, 0, Eps1, 1, Sig1, 0, 0 );

CALL( "basic/cubo.udo", Block, bl, bw, bh, smed, E, 0, x, y, z, 11 );

Eps1 = Epsilon1;
Eps2 = Epsilon2;
Sig = 2.45*Eps2/18;

CALL( "basic/sp.udo", mysp, 2*r0, 16, metal, "N", 2, x+x0, y+y0, z+z0+(bh/2), 10 );

# PORTS
CALL("ports/portoy.udo", oname@port1, Wn, Ww, UP, 1, 25, doubletport1,
     x-Ww/2, y-Ww/2-Wt,z, 11);
CALL("ports/portox.udo", oname@port2, Wn, Ww, DOWN, 2, 25, doubletport2,
     x+Ww/2+Wt, y-Ww/2, z, 11);
CALL("ports/portox.udo", oname@port3, Wn, Ww, UP, 2, 25, doubletport3,
     x-Ww/2-Wt, y-Ww/2, z, 11);
CALL("ports/portoz.udo", oname@port4, Wn, Ww, DOWN, 2, 25, doubletport4,
     x, y, z+Wn+Wt, 11);

# MESH SNAPPING PLANES

CALL( "elements/speczd.udo", spz1, 1, smeshz, x, y, z+bh, 7 );

CALL( "elements/specxu.udo", spxu, 1, smeshx, x-bl/2, y, z, 7 );
CALL( "elements/specxd.udo", spxd, 1, smeshx, x+bl/2, y, z, 7 );

CALL( "elements/specyu.udo", spyu, 1, smeshy, x, y-bw/2, z, 7 );
CALL( "elements/specyd.udo", spyd, 1, smeshy, x, y+bw/2, z, 7 );

CALL( "elements/specx.udo", specx1, 1, x+x0-r0, y, z, 6 );
CALL( "elements/specx.udo", specx2, 1, x+x0+r0, y, z, 6 );
CALL( "elements/specy.udo", specy1, 1, x, y+y0-r0, z, 6 );
CALL( "elements/specy.udo", specy2, 1, x, y+y0+r0, z, 6 );

MESHPAR(cx, cy, cz, 0, 1, 0, 1, 0, 1, 1);

CLOSEOBJ;
```

A.2 15 Test Points in Reconstruction of Four Parameters

ZrO₂ Inclusion

	Parameters:	x0 (mm)	y0 (mm)	z0 (mm)	r0 (mm)
Test 1	Actual:	-12.23	-17.70	5.31	4.35
	Reconstructed:	-11.63	-17.49	5.09	4.49
	% error:	1.01	0.35	0.56	2.94
Test 2	Actual:	-5.04	-4.91	2.49	7.92
	Reconstructed:	-4.95	-6.63	0.27	7.86
	% error:	0.16	2.87	5.53	1.18
Test 3	Actual:	7.60	2.42	0.37	3.32
	Reconstructed:	8.38	3.93	0.73	3.24
	% error:	1.30	2.52	0.89	1.67
Test 4	Actual:	-4.15	-13.45	-1.63	7.47
	Reconstructed:	-4.30	-18.28	-2.68	7.49
	% error:	0.24	8.05	2.63	0.53
Test 5	Actual:	-4.55	-12.14	-4.28	5.53
	Reconstructed:	-3.96	-11.37	-4.61	5.45
	% error:	0.98	1.27	0.82	1.46
Test 6	Actual:	-8.40	1.63	-3.43	3.77
	Reconstructed:	-5.38	0.14	-3.00	3.79
	% error:	5.04	2.48	1.08	0.37
Test 7	Actual:	10.95	-3.93	1.40	5.12
	Reconstructed:	11.47	-3.96	1.65	5.14
	% error:	0.87	0.04	0.63	0.44
Test 8	Actual:	-3.65	-2.62	8.94	5.17
	Reconstructed:	-4.24	-2.37	9.07	5.20
	% error:	0.98	0.42	0.33	0.57
Test 9	Actual:	12.36	12.54	7.38	4.12
	Reconstructed:	11.84	13.98	7.57	4.20
	% error:	0.86	2.39	0.47	1.66
Test 10	Actual:	-14.29	-14.59	-7.11	5.16
	Reconstructed:	-13.78	-12.33	-4.30	4.94
	% error:	0.84	3.75	7.03	4.53
Test 11	Actual:	-6.40	16.22	4.14	6.17
	Reconstructed:	-6.52	17.82	3.30	6.29
	% error:	0.21	2.66	2.09	2.39

SiC Inclusion

	Parameters:	x0 (mm)	y0 (mm)	z0 (mm)	r0 (mm)
Test 1	Actual:	-10.57	-14.00	3.61	7.80
	Reconstructed:	-4.20	-11.75	4.81	7.89
	% error:	10.61	3.74	2.98	1.94
Test 2	Actual:	16.06	-2.69	3.28	4.48
	Reconstructed:	12.79	-3.05	4.35	4.39
	% error:	5.45	0.59	2.67	1.65
Test 3	Actual:	-0.36	18.95	-7.03	4.15
	Reconstructed:	-0.87	13.09	-8.28	4.29
	% error:	0.84	9.76	3.13	2.79
Test 4	Actual:	-2.59	-8.86	-10.27	5.72
	Reconstructed:	-2.07	-8.19	-8.12	5.55
	% error:	0.86	1.12	5.37	3.32
Test 5	Actual:	11.47	-13.66	-2.62	6.44
	Reconstructed:	12.82	-11.20	-4.15	6.38
	% error:	2.25	4.11	3.84	1.34
Test 6	Actual:	-10.55	-12.19	-0.10	5.24
	Reconstructed:	-11.01	-11.71	0.31	5.18
	% error:	0.76	0.80	1.01	1.24
Test 7	Actual:	-12.14	-11.64	-11.47	7.51
	Reconstructed:	-11.27	-6.95	-9.61	7.34
	% error:	1.45	7.82	4.65	3.32
Test 8	Actual:	-10.40	-15.30	-9.42	3.94
	Reconstructed:	-11.69	-13.92	-8.88	3.85
	% error:	2.13	2.30	1.35	1.83
Test 9	Actual:	4.74	-10.95	6.21	6.63
	Reconstructed:	4.41	-11.89	5.48	6.60
	% error:	0.56	1.58	1.82	0.63
Test 10	Actual:	8.63	8.78	-2.52	4.18
	Reconstructed:	6.56	5.89	-3.40	4.19
	% error:	3.44	4.82	2.19	0.17
Test 11	Actual:	-14.59	22.70	-1.67	7.85
	Reconstructed:	-10.99	16.65	0.57	8.00
	% error:	6.01	10.08	5.62	2.88

	Parameters:	x0 (mm)	y0 (mm)	z0 (mm)	r0 (mm)
	Actual:	2.48	6.90	5.39	6.64
Test 12	Reconstructed:	2.78	6.59	4.62	6.64
	% error:	0.49	0.52	1.94	0.03

	Parameters:	x0 (mm)	y0 (mm)	z0 (mm)	r0 (mm)
	Actual:	-0.04	-4.02	-5.33	6.45
Test 13	Reconstructed:	1.09	-6.19	-6.88	6.41
	% error:	1.88	3.61	3.86	0.83

	Parameters:	x0 (mm)	y0 (mm)	z0 (mm)	r0 (mm)
	Actual:	-5.67	-0.59	1.44	5.92
Test 14	Reconstructed:	-4.99	-0.79	1.91	5.87
	% error:	1.13	0.33	1.19	0.89

	Parameters:	x0 (mm)	y0 (mm)	z0 (mm)	r0(mm)
	Actual:	-0.85	0.16	-0.71	5.66
Test 15	Reconstructed:	-1.18	1.01	0.43	5.70
	% error:	0.54	1.42	2.86	0.73

Parameters:	x0 (mm)	y0 (mm)	z0 (mm)	r (mm)
Average % Error	1.10	2.18	2.13	1.35

	Parameters:	x0 (mm)	y0 (mm)	z0 (mm)	r0 (mm)
	Actual:	-9.57	-15.19	1.54	3.68
Test 12	Reconstructed:	-8.70	-17.94	3.25	3.69
	% error:	1.45	4.59	4.26	0.19

	Parameters:	x0 (mm)	y0 (mm)	z0 (mm)	r0 (mm)
	Actual:	-12.15	13.86	6.02	4.64
Test 13	Reconstructed:	-10.12	14.18	4.67	4.62
	% error:	3.38	0.53	3.37	0.39

	Parameters:	x0 (mm)	y0 (mm)	z0 (mm)	r0 (mm)
	Actual:	-20.69	-25.26	4.85	7.85
Test 14	Reconstructed:	-10.32	-15.91	4.59	7.79
	% error:	17.28	15.58	0.65	1.25

	Parameters:	x0 (mm)	y0 (mm)	z0 (mm)	r0(mm)
	Actual:	13.62	0.59	-5.71	4.95
Test 15	Reconstructed:	12.91	-1.47	-4.51	4.86
	% error:	1.19	3.43	3.01	1.93

Parameters:	x0 (mm)	y0 (mm)	z0 (mm)	r (mm)
Average % Error	3.84	4.72	3.06	1.66

Metal Inclusion

	Paramters:	x0 (mm)	y0 (mm)	z0 (mm)	r0 (mm)
	Actual:	7.76	-7.15	-2.03	3.34
Test 1	Reconstructed:	12.09	-8.72	-1.69	3.12
	% error:	7.21	2.62	0.85	4.40

	Paramters:	x0 (mm)	y0 (mm)	z0 (mm)	r0 (mm)
	Actual:	-7.35	-8.00	9.59	5.29
Test 2	Reconstructed:	-6.21	-6.29	9.68	5.23
	% error:	1.90	2.84	0.23	1.15

	Paramters:	x0 (mm)	y0 (mm)	z0 (mm)	r0 (mm)
	Actual:	5.35	-10.35	-6.71	3.86
Test 3	Reconstructed:	4.17	-8.35	-6.04	3.88
	% error:	1.97	3.33	1.67	0.43

	Paramters:	x0 (mm)	y0 (mm)	z0 (mm)	r0 (mm)
	Actual:	-73.96	-30.88	-18.96	4.71
Test 4	Reconstructed:	-3.90	-13.54	1.07	5.32
	% error:	116.77	28.91	50.07	12.17

	Paramters:	x0 (mm)	y0 (mm)	z0 (mm)	r0 (mm)
	Actual:	-2.42	4.03	6.70	7.62
Test 5	Reconstructed:	-6.67	2.30	8.75	7.89
	% error:	7.08	2.89	5.13	5.27

	Paramters:	x0 (mm)	y0 (mm)	z0 (mm)	r0 (mm)
	Actual:	11.47	-0.44	-1.62	4.39
Test 6	Reconstructed:	7.98	-1.08	-2.26	4.34
	% error:	5.82	1.07	1.59	0.94

	Paramters:	x0 (mm)	y0 (mm)	z0 (mm)	r0 (mm)
	Actual:	6.44	-4.61	1.13	3.36
Test 7	Reconstructed:	14.16	-15.26	9.75	3.02
	% error:	12.87	17.74	21.57	6.85

	Paramters:	x0 (mm)	y0 (mm)	z0 (mm)	r0 (mm)
	Actual:	8.64	7.68	-1.08	3.47
Test 8	Reconstructed:	14.16	10.87	-0.40	3.34
	% error:	9.20	5.32	1.69	2.55

	Paramters:	x0 (mm)	y0 (mm)	z0 (mm)	r0 (mm)
	Actual:	6.68	1.37	6.40	7.53
Test 9	Reconstructed:	3.93	5.27	9.35	7.52
	% error:	4.58	6.49	7.37	0.20

	Paramters:	x0 (mm)	y0 (mm)	z0 (mm)	r0 (mm)
	Actual:	-8.60	7.25	7.36	6.43
Test 10	Reconstructed:	-8.94	9.10	8.00	6.47
	% error:	0.56	3.08	1.59	0.72

	Paramters:	x0 (mm)	y0 (mm)	z0 (mm)	r0 (mm)
	Actual:	-4.98	11.67	-7.18	5.31
Test 11	Reconstructed:	-4.14	10.06	-6.69	5.25
	% error:	1.41	2.68	1.23	1.07

	Paramters:	x0 (mm)	y0 (mm)	z0 (mm)	r0 (mm)
	Actual:	-2.52	-7.15	3.32	3.45
Test 12	Reconstructed:	-2.53	-10.09	4.02	3.34
	% error:	0.01	4.89	1.76	2.29

	Paramters:	x0 (mm)	y0 (mm)	z0 (mm)	r0 (mm)
	Actual:	2.59	-4.77	-0.58	7.13
Test 13	Reconstructed:	4.74	-4.90	-2.33	7.14
	% error:	3.59	0.21	4.40	0.14

	Paramters:	x0 (mm)	y0 (mm)	z0 (mm)	r0 (mm)
	Actual:	6.43	3.08	-1.83	3.16
Test 14	Reconstructed:	15.54	15.70	1.49	3.10
	% error:	15.18	21.03	8.30	1.30

	Paramters:	x0 (mm)	y0 (mm)	z0 (mm)	r0(mm)
	Actual:	11.09	19.32	6.75	5.00
Test 15	Reconstructed:	9.17	15.46	7.05	4.86
	% error:	3.20	6.44	0.75	2.86

Paramters	x0 (mm)	y0 (mm)	z0 (mm)	r (mm)
Average % Error	**12.76**	**7.30**	**7.21**	**2.82**

A.2 15 Test Points in Reconstruction of Six Parameters

Dielectric Inclusion

	Paramters:	x0 (mm)	y0 (mm)	z0 (mm)	r0 (mm)	eps'	eps"
	Actual:	9.76	-8.18	-6.64	7.98	10.47	0.75
Test 1	Reconstructed:	6.40	16.18	9.87	7.70	12.51	1.27
	% error:	5.59	40.60	41.30	5.48	34.13	52.05
	Paramters:	x0 (mm)	y0 (mm)	z0 (mm)	r0 (mm)	eps'	eps"
	Actual:	12.63	14.34	-6.28	4.54	11.27	0.90
Test 2	Reconstructed:	12.73	14.25	-6.12	4.57	11.08	0.82
	% error:	0.17	0.15	0.40	0.57	3.25	8.26
	Paramters:	x0 (mm)	y0 (mm)	z0 (mm)	r0 (mm)	eps'	eps"
	Actual:	-3.10	6.46	4.10	5.44	11.12	0.73
Test 3	Reconstructed:	-2.60	7.09	2.59	5.46	10.91	0.78
	% error:	0.83	1.05	3.78	0.32	3.51	5.19
	Paramters:	x0 (mm)	y0 (mm)	z0 (mm)	r0 (mm)	eps'	eps"
	Actual:	-0.83	-3.11	6.06	4.07	10.66	0.90
Test 4	Reconstructed:	-0.76	-3.28	7.04	4.16	10.54	0.82
	% error:	0.11	0.29	2.45	1.83	1.93	8.72
	Paramters:	x0 (mm)	y0 (mm)	z0 (mm)	r0 (mm)	eps'	eps"
	Actual:	-3.65	15.32	-4.66	7.52	8.75	0.55
Test 5	Reconstructed:	-1.86	15.98	0.63	7.30	9.77	0.74
	% error:	2.99	1.10	13.20	4.48	16.99	19.29
	Paramters:	x0 (mm)	y0 (mm)	z0 (mm)	r0 (mm)	eps'	eps"
	Actual:	-12.54	-4.71	-1.36	3.27	12.55	0.70
Test 6	Reconstructed:	-8.77	-6.98	-0.48	3.31	10.99	0.91
	% error:	6.28	3.79	2.18	0.73	26.07	21.45
	Paramters:	x0 (mm)	y0 (mm)	z0 (mm)	r0 (mm)	eps'	eps"
	Actual:	5.42	-10.37	-3.34	4.63	10.90	1.22
Test 7	Reconstructed:	6.23	-14.62	-3.67	4.54	9.97	1.09
	% error:	1.35	7.08	0.84	1.78	15.51	13.25
	Paramters:	x0 (mm)	y0 (mm)	z0 (mm)	r0 (mm)	eps'	eps"
	Actual:	-10.56	12.83	4.25	3.51	12.49	1.48
Test 8	Reconstructed:	-10.21	9.24	3.75	3.70	10.17	0.98
	% error:	0.59	5.97	1.25	3.85	38.66	50.81
	Paramters:	x0 (mm)	y0 (mm)	z0 (mm)	r0 (mm)	eps'	eps"
	Actual:	0.99	-12.92	7.29	4.22	7.09	1.33
Test 9	Reconstructed:	0.51	-11.18	7.01	4.26	7.55	1.22
	% error:	0.79	2.90	0.70	0.79	7.66	11.06
	Paramters:	x0 (mm)	y0 (mm)	z0 (mm)	r0 (mm)	eps'	eps"
	Actual:	1.22	13.12	-3.84	4.52	9.91	0.54
Test 10	Reconstructed:	1.10	20.71	-3.11	4.40	12.44	0.95
	% error:	0.21	12.64	1.84	2.45	42.11	41.48
	Paramters:	x0 (mm)	y0 (mm)	z0 (mm)	r0 (mm)	eps'	eps"
	Actual:	4.29	-19.73	-9.32	5.54	8.42	0.83
Test 11	Reconstructed:	5.26	-26.59	-9.39	5.24	9.85	1.06
	% error:	1.63	11.44	0.19	6.03	23.80	23.10

	Paramters:	x0 (mm)	y0 (mm)	z0 (mm)	r0 (mm)	eps'	eps"
	Actual:	4.77	19.54	-4.10	5.01	12.23	0.95
Test 12	Reconstructed:	3.26	18.18	-4.54	5.15	11.39	0.90
	% error:	2.50	2.27	1.09	2.70	14.07	4.08

	Paramters:	x0 (mm)	y0 (mm)	z0 (mm)	r0 (mm)	eps'	eps"
	Actual:	-8.06	-2.14	-4.38	6.71	11.38	1.36
Test 13	Reconstructed:	-9.69	-3.53	-4.75	6.87	9.86	1.05
	% error:	2.71	2.33	0.91	3.18	25.37	31.63

	Paramters:	x0 (mm)	y0 (mm)	z0 (mm)	r0 (mm)	eps'	eps"
	Actual:	-9.30	1.70	-8.71	6.08	7.75	1.40
Test 14	Reconstructed:	-8.22	-3.49	-8.29	6.61	4.85	1.27
	% error:	1.80	8.66	1.05	10.58	48.35	13.34

	Paramters:	x0 (mm)	y0 (mm)	z0 (mm)	r0(mm)	eps'	eps"
	Actual:	14.82	-6.84	5.06	5.34	12.94	1.10
Test 15	Reconstructed:	13.15	-5.06	3.65	5.39	11.91	0.98
	% error:	2.78	2.96	3.52	1.00	17.07	11.72

Paramters	x0 (mm)	y0 (mm)	z0 (mm)	r (mm)	eps'	eps"
Average % Error	2.02	6.88	4.98	3.05	21.23	21.03

References

[1] T. Kundu, Ed., *Ultrasonic and Electromagnetic NDE for Structure and Material Characterization: Engineering and Biomedical Applications*, CRC Press, 2012.

[2] L.W. Schmerr, *Fundamentals of Ultrasonic Nondestructive Evaluation: A Modeling Approach*, Springer, 2016.

[3] G. Huebschen, I. Altpeter, R. Tschuncky, and H.-G. Herrmann, Eds., *Materials Characterization Using Nondestructive Evaluation Methods*, Woodhead Publishing, 2016.

[4] R. Zoughi, *Microwave Non-Destructive Testing and Evaluation*, Kluwer, 2000.

[5] N. Nikolova, *Microwave Biomedical Imaging*. In: *Wiley Encyclopedia of Electrical and Electronics Engineering*, J. Webster Ed., 2014, pp. 1-22.

[6] X. Li, S.K. Davis, S.C. Hagness, D.W. van der Weide, and B.D. Van Veen, Microwave imaging via space-time beamforming: Experimental investigation of tumor detection in multilayer breast phantoms, *IEEE Trans. Microwave Theory Tech.*, vol. 52, no 8, pp. 1856–1865, 2004.

[7] G. Bindu and K. T. Mathew, Characterization of behind and malignant breast tissues using 2-D microwave tomographic imaging, *Microwave Opt. Technol. Lett.*, vol. 49, no 10, pp. 2341–2345, 2004.

[8] K. Belkebir, R. E. Kleinman, and C. Pichot, Microwave imaging—Location and shape reconstruction from multi-frequency scattering data, *IEEE Trans. Microwave Theory Tech.*, vol. 45, no 4, pp. 469–476, Apr. 1997.

[9] N. Qaddoumi, G. Carriveau, S. Ganchev, and R. Zoughi, Microwave imaging of thick composite panels with defects, *Mater. Eval.,* vol. 53, no 8, pp. 926–929, 1995.

[10] M. Pastorino, A. Salvade, R. Monleone, T. Bartesaghi, G. Bozza, and A. Randazzo, Detection of defects in wood slabs by using a microwave imaging technique*, IEEE Instrum. Meas. Tech. Conf.*, pp. 1–6, 2007.

[11] G. Mohammad T. A., Real-time and portable microwave imaging system. *Doctoral Dissertations. Paper 2247*, 2009.

[12] A. V. Brovko, E. K. Murphy, and V. V. Yakovlev, Waveguide microwave imaging: neural network reconstruction of functional 2-D permittivity profiles, *IEEE Trans. Microwave Theory Tech*., vol. 57, no 2, pp. 406-414, 2009.

[13] D. Colton and R. Kress, *Inverse Acoustic and Electromagnetic Scattering Theory*. Springer, 1998.

[14] T. Meyer, A. Jostingmeier, and A. S. Omar, Microwave imaging using a novel regularization scheme*, IEEE AP-S Int. Symp. Dig.*, vol. 3, pp. 175–178, 2003.

[15] Yu.V. Shestopalov and V.V. Yakovlev, Uniqueness of complex permittivity reconstruction in a parallel-plane waveguide, *Radio Science*, vol. 42, RS6S20, 2007.

[16] Yu.V. Shestopalov and Yu.G. Smirnov, Determination of permittivity of an inhomogeneous dielectric body in a waveguide, *Inverse Problems*, vol. 27, no 9, 2011.

[17] Yu.G. Smirnov, Yu.V. Shestopalov, E. Derevyanchuk, Inverse problem method for complex permittivity reconstruction of layered media in a rectangular waveguide*, Physica Status Solidi.*, vol. 11, no 5-6, pp. 969-974, 2014.

[18] K. Belkebir, R. E. Kleinman, and C. Pichot, Microwave imaging – Locations and shape reconstruction from multifrequency scattering data*, IEEE Trans. Microw. Theory Tech.,* vol. 45, no. 4, pp. 469–476, Apr. 1997.

[19] A. J. Bahr, R. Zoughi, and N. Qaddoumi, *Microwave, Non-Destructive Evaluation. Theory, Techniques, and Applications,* P. J. Shull, Ed. Marcel Dekker, 2002.

[20] S. L. Taylor, *Advances in Food and Nutrition Research*. Academic Press*,* vol. 51, 2006.

[21] A. Lonappan, Novel method of detecting pregnancy using microwaves, *J. Electromag. Analysis and Appl*., vol. 4, pp. 340-343, 2012.

[22] S. Chainon and M. Himdi, Transmission line model for longitudinal slot dielectric-filled waveguide, *IEEE AP-S Intern. Symp.*, pp. 424-427, June 2002.

[23] V.V. Komarov and V.V. Yakovlev, CAD of efficient TM_{mn0} single-mode elliptical applicators with coaxial excitation, *J. Microwave Power & Electromag. Energy*, vol. 40, no. 3, pp. 174-185. 2007

[24] A. Smirnov, A. Semenov and Yu.V. Shestopalov, Modeling of electromagnetic wave propagation in guides with inhomogeneous dielectric inclusions, *Springer Proceedings in Mathematics & Statistics*, vol. 52, pp. 113-118, 2013.

[25] D. Xu, Z. Li, X. Chen, Z. Wang, and J. Wu, A dielectric-filled waveguide antenna element for 3D imaging radar in high temperature and excessive dust conditions, *Sensors, 2016*, vol. 16, p. 1339, 2016.

[26] D.M. Sullivan, *Electromagnetic Simulation Using the FDTD Method*, IEEE Press, 2000.

[27] U.S. Inan and R.A. Marshall, *Numerical Electromagnetics. The FDTD Method*, Cambridge University Press, 2011.

[28] V.V. Komarov and V.V. Yakovlev, Modeling control over determination of dielectric properties by perturbation technique, *Microwave Opt. Tech. Letters*, vol. 39, no 6, pp. 443-446, 2003.

[29] M. Celuch and W.K. Gwarek, Properties of the FDTD method relevant to the analysis of microwave power problems, J. *Microwave Power and Electromag. Energy*, vol. 41, no 4, pp. 62-80, 2007.

[30] M.H. Hassoun, *Artificial Neural Networks,* MIT Press, 1995.

[31] S. Haykin,*Neural Networks A Comprehensive Foundation*, Prentice-Hall, Inc., 1999.

[32] A.V. Brovko, E.K. Murphy, and V.V. Yakovlev, Waveguide microwave imaging: solids volume fraction of particulate materials, *ACES J.*, vol. 30, no 11, pp. 2015.

[33] A.V. Brovko, E.K. Murphy, M. Rother, H.P. Schuchman, and V.V. Yakovlev, Waveguide microwave imaging: spherical inclusion in a dielectric sample, *IEEE Microwave and Wireless Components Letters*, vol. 18, no 9, pp. 647- 649, 2008.

[34] A.V. Brovko, E.K Murphy, and V.V. Yakovlev. Modeling-based technique for 3D permittivity profile reconstruction, *Proc. 47th IMPI's Microwave Power Symp. (Providence, RI, June 2013)*, pp. 97-100.

[35] T.V. Koutchma and V.V. Yakovlev, Computer modeling of microwave heating processes for food preservation, In: M.M. Farid, Ed., *Mathematical Analysis of Food Processing*, CRC Press, 2010, pp. 625-657.

[36] *QuickWave 2016™*, QWED Sp. z o. o., http://www.qwed.com.pl/.

[37] E. K. Murphy and V. V. Yakovlev, RBF network optimization of complex microwave systems represented by small FDTD modeling data sets, *IEEE Trans. Microw. Theory Tech.*, vol. 54, no 7, pp. 3069-3083, 2006.